

American University in Cairo

AUC Knowledge Fountain

Theses and Dissertations

Student Research

Spring 6-11-2020

A patient-specific adaptation of the Living Human Heart Model in application to pulmonary hypertension

Yousof Abdel-Raouf

The American University in Cairo

Follow this and additional works at: <https://fount.aucegypt.edu/etds>

Recommended Citation

APA Citation

Abdel-Raouf, Y. (2020). *A patient-specific adaptation of the Living Human Heart Model in application to pulmonary hypertension* [Master's Thesis, the American University in Cairo]. AUC Knowledge Fountain. <https://fount.aucegypt.edu/etds/1467>

MLA Citation

Abdel-Raouf, Yousof. *A patient-specific adaptation of the Living Human Heart Model in application to pulmonary hypertension*. 2020. American University in Cairo, Master's Thesis. *AUC Knowledge Fountain*. <https://fount.aucegypt.edu/etds/1467>

This Master's Thesis is brought to you for free and open access by the Student Research at AUC Knowledge Fountain. It has been accepted for inclusion in Theses and Dissertations by an authorized administrator of AUC Knowledge Fountain. For more information, please contact thesisadmin@aucegypt.edu.

The American University in Cairo

School of Science and Engineering

Biotechnology Program



***A Patient Specific Adaptation of the
Living Human Heart Model in
Application to Pulmonary Hypertension***

By:

Yousof Mohamed Assaad Abdel-Raouf

A thesis submitted in partial fulfillment of the
degree

Masters of Science in Biotechnology

Under the Supervision of

Dr. Khalil Elkhodary

Associate Professor

Department of Mechanical Engineering,
School of Sciences and Engineering
The American University in Cairo

Dr. Mohamed Badran

Assistant Professor

Mechanical Engineering
Department,
Faculty of Engineering & Technology
Future University in Egypt

Dr. Alireza Heidari

Research Associate

Department of Mathematics &
Statistics, Faculty of Science
Department of Anatomy and Cell
Biology, Faculty of Medicine
McGill University

Abstract

The Living Heart Project aims to offer medical practitioners and researchers a full-heart electromechanical computational platform to explore and assess clinical cases pertaining to the left ventricle (LV), and the less addressed right ventricle (RV). It does not, however, provide an easy solution to applying this platform to patient-specific cases that account for a large variability among cases. We, therefore, present a solution to modify the Living Human Heart Model (LHHM) to obtain a patient-specific geometry using the thermal expansion method, with iteratively adjusted parameters that accurately simulate the case of a 72-year-old female patient suffering from secondary pulmonary hypertension caused by mitral valve regurgitation (MR). The patient underwent MV replacement and we simulate the heart from magnetic resonance imaging (MRI) images prior to surgery and 3 days following surgery. A mean pulmonary arterial pressure (mPAP) of approximately 64 mmHg was demonstrated before surgery, along with a severe lack of coaptation of the mitral valve. Reduced function of the cardiac chambers is exhibited in the reduced ejection fraction (EF). We also demonstrate left-side failure, an increase in Global Longitudinal Strain (GLS) and the location of maximum cardiac wall stress located at the mid anterolateral wall of the RV where dilation traditionally manifests. Comparison of patient geometry pre-operation and post-surgery showed a change in shape of the Tricuspid Annulus (TA) in systole. A rigid constraint across the TA was used to simulate an annuloplasty ring, and an increase in ring-widening forces was observed post-operation, with a significant reduction in forces being present in contractile forces on the ring. This model led us to conclude that the patient will likely develop TV annular dilatation and subsequent regurgitation in the absence of intervention. We verify the use of the LHHM for assessing potential remodeling and subclinical RV dysfunction, and subsequent intervention and attenuation of pulmonary hypertension by a mitral valve replacement. The lack of personalization and wide variability have remained a significant reason for the slow adoption rate of computational tools among medical practitioners, but we see this work as a substantial addition to computational cardiology, and foresee a closer integration of such technology to mainstream application among members of the medical community.

Acknowledgement

I wish here to acknowledge the tremendous effort of those around me who have given support, guidance, encouragement and patience without limit. First and foremost, I would like to express my gratitude towards my advisors, Dr. Khalil El-Khodary, Dr. Mohamed Badran and Dr. Alireza Heidari for their professional and personal insight and mentorship throughout my studies at AUC. I would also like to thank the members of the Biotechnology Program, including Dr. Asma Amleh, Dr. Ahmed Moustafa and Prof. Hassan El-Fawal, and their endless support inside and outside the classroom. Additionally, I would be at fault not to mention the help and support of my colleagues and members of the research team, namely Noha Shalaby, Antony Assaad and Andrew Youssef. Moreover, I realize that it would not have been possible to pursue my degree without the aide and care of the members of the Al-Alfi foundation. Finally, I wish to express in a few humble words my gratitude towards my family and friends who have accompanied me on this journey. I continue to be inspired and thankful for my father's wisdom and mother's patience, as well as my brother's drive, and the love and support of my friends Amal, Manar, Othman, Sara and Sherif who picked me up when I was down.

List of Abbreviations:

Acronym	Description
ADP	Adenosine Diphosphate
ATP	Adenosine Triphosphate
AV	Aortic Valve
AVN	Atrioventricular Node
CFD	Computational Fluid Dynamics
CMR	Cardiac Magnetic Resonance
CO	Cardiac Output
EDV	End Diastolic Volume
EF	Ejection Fraction
ESV	End Systolic Volume
HF	Heart Failure
FE	Finite Element Method
FSI	Fluid-Structure Interaction
FTR	Functional Tricuspid Regurgitation
GLS	Global Longitudinal Strain
LA	Left Atrium
LHHM	Living Human Heart Model
LHP	Living Heart Project
LV	Left Ventricle
MA	Mitral Annulus
mPAP	Mean Pulmonary Arterial Pressure
MR	Mitral Valve Regurgitation
MRI	Magnetic Resonance Imaging
MV	Mitral Valve
PAP	Pulmonary Arterial Pressure
PH	Pulmonary Hypertension
PM	Papillary Muscle
PV	Pulmonary Valve
RA	Right Atrium
RV	Right Ventricle
SA	Sinoatrial Node
SEF	Strain Energy Function
TA	Tricuspid Annulus
TAPSE	Tricuspid Annular Systolic Excursion
TR	Tricuspid Regurgitation
TTE	Transthoracic Echocardiography
TV	Tricuspid Valve

Table of Contents

Abstract	I
Acknowledgement	II
List of Abbreviations:	III
Table of Figures	VI
List of Tables	VIII
1. Introduction	1
1.1 Thesis Contribution	2
1.2 Thesis Organization	2
2. Literature Review	3
2.1 Overview of Cardiac System	3
2.2 Pathologies of Interest	10
2.2.1 Pulmonary Hypertension	10
2.2.2 Functional Tricuspid Regurgitation	11
2.3 Computational Assessment of Pulmonary Hypertension and Regurgitant Valves	14
2.3.1 Pulmonary Hypertension	14
2.3.2 Functional Tricuspid Regurgitation	18
2.4 The Living Human Heart Model	21
2.4.1 Geometry and Framework	21
2.4.2 Electrical Modelling	23
2.4.3 Mechanical Modelling	24
3. Methodology	27
3.1 Reverse Remodeling	27
3.1.1 Patient Specific Data Acquisition	27
3.1.2 Parametric Study: LA Dilation	30
3.1.3 Adjustment of Material Properties	33
3.2 TV Investigation	34
3.2.1 TA Forces	34
4. Results & Discussion	36
5. Conclusion & Future Works	49
References	51
Appendix	60
1.1 Overview of Continuum Models	60

1.2	Abaqus Implementation _____	62
1.3	Parameters Used in our model _____	64
1.4	Measured Raw Data Fitting/Shape Analysis _____	66

Table of Figures

<i>Figure 1 A diagram illustrating (Left) The major chambers and vasculature of the heart and (Right) the underlying musculature of the heart</i>	<u>3</u>
<i>Figure 2 A schematic (Left) showing the underlying pacemaker cells and Purkinje Fibers as well as the major components of the conduction system. (Right) graph of potential in one beat.</i>	<u>5</u>
<i>Figure 3 A schematic of striated myofibers and the process of contraction. The influx of Calcium ions during depolarization allows for unbinding of the actin-troponin-myosin complex, and phosphorylation of the actin-myosin complex causes contraction</i>	<u>7</u>
<i>Figure 4 The Frank-Starling Effect shows the range of length at which active myofiber forces can be created. The length between a and b is optimum due to a large overlap between actin and myosin fibers, which maintains and increases contractility. Adapted from (Shiels and White, 2008)</i>	<u>7</u>
<i>Figure 5 Example of Pressure-Volume Loop and their corresponding place in the cardiac cycle</i>	<u>9</u>
<i>Figure 6 The saddle shape associated with a healthy TA is made more flattened and circular. Right side failure often associated with RA and RV dilation causes an increase in annulus size in the lateral direction. Adapted from (Bessler, Meduli and Lurz, 2017)</i>	<u>13</u>
<i>Figure 7 Geometry of 25-year-old healthy male heart used in LHHM (left). Superimposed Fiber Orientation (Right). Red - Epicardial Fiber. Green - Mid Myocardial Fibers. Blue - Endocardial Fibers</i>	<u>22</u>
<i>Figure 8 Implementation of Biochemical Model. Different graphs correspond to different refractoriness characteristic of tissue properties</i>	<u>24</u>
<i>Figure 9 Time-Dependent Active stress. Shaded lines imply a longer relaxation time associated with increased Fiber strain. Arrow represents active stress curve at minimum strain</i>	<u>26</u>
<i>Figure 10 MRI obtained images of patient heart Pre-surgery (a) Shows a 3D volume of the patient chest generated in MATLAB (b) A four-chamber view showing an enlarged RA (c) Short-axis biventricular view with a flattened septum and characteristic D-shaped LV (d) Left-heart view of the LA and LV</i>	<u>29</u>
<i>Figure 11 Illustration of Purkinje fiber reconstruction overlaid on-top of the two-chamber slice of the ventricles. When ventricles are morphed, zero distance is kept between ventricular geometry and Purkinje fiber geometry</i>	<u>31</u>
<i>Figure 12 Flow-Chart of Expansion Method applied to simulate Dilation</i>	<u>32</u>
<i>Figure 13 TAPSE is measured as the difference between maximum and minimum lengths in the M-mode (shown in red) (a,b) through the cardiac cycle. Six segments of the RV Free wall have been used to extract circumferential and longitudinal strain (c)</i>	<u>33</u>
<i>Figure 14 Rigid Links shown in red (a), along with link formulation (b). Links maintain kinematic motion between points a and b (in this case our suture points)</i>	<u>35</u>

<i>Figure 15 Contour plot interpolating the relationship between RA volume, Temperature applied for thermal expansion, and Preload Pressure. Our model correctly predicts values where preload pressure is high, regardless of applied temperature</i>	36
<i>Figure 16 End Diastolic patient geometry pre-surgery in a left side view (a,b) and a 4-chamber view (c,d). A limitation of thoracic-chest CMR imaging lies in the patient stillness during 45 -50-minute sessions. Paraview was used to define the location of the cuts. Since the MRI cuts were midpoints between frames, the 3D model cuts were taken across the center of the heart.</i>	38
<i>Figure 17 Stress distribution in the End Diastolic pulmonary trunk shows an increase in stress and bulging of the compliant artery in the case of elevated mPAP.</i>	39
<i>Figure 18 Pulmonary pressure profile shows the difference between pulmonary pressure in our model and the increase in peakPAP/mPAP ratio after surgery due to left-side failure relief</i>	39
<i>Figure 19 Atrial view of the mid-systolic biventricular pre-operation geometry. Meshing of the ventricles, valves and chordae is shown and incomplete coaptation of the MV can be seen. RA and LA geometries were removed for clarity.</i>	40
<i>Figure 20 LV cardiac output parameters in our model demonstrated along with data from (Xi et al., 2017). The remarkable reduction in LV volume after removal of the afterload is visible.</i>	40
<i>Figure 21 Profile describing Circumferential and longitudinal strain compared to data reported in (Xi et al., 2017) and (Finsberg et al., 2019) respectively.</i>	41
<i>Figure 22 RV mid-systolic stress in the RVFW shows higher stresses in regions corresponding to PH associated shape change in (Leary et al., 2012; Mertens and Hunter, 2012)</i>	42
<i>Figure 23 Transmural End-Systolic stress and strain of the ventricles at the mid-myocardium. Stresses are much higher in the Pre-Surgery indicating location of possible dilation in RV (black arrow)</i>	43
<i>Figure 24 Transmural End Diastolic stress and strain of the ventricles at the mid-myocardium. LV stress is increased after surgery due to the Frank-Starling effect</i>	44
<i>Figure 25 Mid-systolic stress (a,b) and strain (c,d) distribution in TV/MV and ventricles in pre-operation and post-operation. The replacement of the MV with an annuloplasty ring shows a clear reduction in stress and strain at the Mitral Annulus (MA)</i>	45
<i>Figure 26 Comparison of forces on the TA shows a higher diastolic force post-operation suggesting TA dilation is more likely. Reduced force during systole also suggests a loss of the role of the TA in coaptation</i>	46
<i>Figure 27 The location of the TA sections exhibiting the largest forces in pre-operation and post-operation geometries. (white)</i>	46
<i>Figure 28 A graph of total forces on rigid and semi-rigid rings shows a reduction of forces during the contraction, reflecting a reduced likelihood of dehiscence – or suture would trauma.</i>	47

List of Tables

<i>Table 1 Breakdown of the Cardiac Cycle</i>	8
<i>Table 2 Summary of Computational Modelling of FTR</i>	20
<i>Table 3 MRI report of patient End Diastolic Volume, Stroke Volume and Ejection Fraction compared to values in healthy female patients of mean age 43 reported in (Lin et al. 2008)</i>	29
<i>Table 4 Comparison of shape indices between MRI images and our model</i>	37
<i>Table 5 Comparison of Forces on constrained Pre-Operative and Post-Operative Geometry</i>	48

1. Introduction

Pulmonary Hypertension (PH) is a disease characterized by the increase in mean pressure in the pulmonary system. The World Health Organization (WHO) classifies patients suffering from hypertension into 5 categories as follows (Galiè, Humbert and Vachiery, 2015):

- WHO Group 1: Pulmonary Arterial Hypertension, which is associated with other diseases such as congenital heart disease or other infectious diseases (e.g. HIV)
- WHO Group 2: Pulmonary Hypertension due to Left Heart Disease, which is associated with left-side heart failure or valve diseases.
- WHO Group 3: Pulmonary Hypertension due to Lung Disease or hypoxia, which is associated with diseased lungs and decreased uptake of oxygen into the blood.
- WHO Group 4: Pulmonary Hypertension due to Lung Vasculature Interruption, which is associated with occlusion or disruption of the vascular bed at the lungs.
- WHO Group 5: Pulmonary Hypertension due to diseases in the Blood, which is associated with systemic diseases and hematological diseases, e.g. sickle cell anemia.

WHO Group 2 composes the largest plurality of those who suffer from hypertension, approximately 50% of the PH cases in the Middle East (2.5 million of 5 million) and globally (Hoepfer et al., 2016). It is of note that women are more widely affected. In general, patients face a 25% increase in mortality with every 5-mmHg increase in pulmonary pressure (Barnett and Selby, 2015).

With the progression of PH disease, the right-side of the heart, which is in direct series to the pulmonary system, is adversely affected and the function of the heart is impaired, likely triggering right-side failure. It is thus important to understand how this progression occurs and what interventions can be made to mitigate the effects of PH and to achieve a better prognosis. Right Ventricular (RV) dilation and Tricuspid Valve (TV) regurgitation are direct effects of severe PH, and no general agreement exists on a diagnosis and intervention in Tricuspid Valve Regurgitation (David, David and Manhiolt, 2015; Shuhaiber, 2018).

1.1 Thesis Contribution

There is today a remarkable need for, and absence of, a comprehensive framework for patient-specific computational assessment of cardio-pathologies. This thesis offers a prospective study in that direction, where we present an assessment of a 72-year-old female patient suffering from PH that was caused by Mitral Valve Regurgitation (MR). The patient underwent Mitral Valve (MV) replacement surgery with a bioprosthetic valve, and was fitted with a TV annuloplasty ring to prevent the onset of TV regurgitation (TR). We here build on the tools developed under the Living Heart Project, i.e. the Living Human Heart Model (LHHM) of Dassault Systèmes, which is not inherently a patient-specific model. We thus present our developed methodology for the adjustment of heart geometry to patient-specific imaging, and our subsequent implementation of patient-specialized Multiphysics simulations that reflect the key disease hallmarks which fully define the state of the heart pre-surgery and post-surgery. We demonstrate that our technique fully characterizes the MR and PH conditions from which the patient suffers, and predicts possible complications caused by the disease, such as TR. We also evaluate the use of our platform as a possible way to test intervention policies to valvopathy in the context of a full-heart simulation.

1.2 Thesis Organization

The Thesis will be presented in five sections, with section 2 presenting a brief explanation of cardiac physiology, an overview of the clinical problem and of efforts made to tackle it, and finally a brief description of the LHHM. Section 3 describes the patient's condition and details the methodology we develop to model it, which we follow up by section 4 to discuss key results of our modelling. Section 5 concludes our work and highlights the limitations and implications of our work, as well as directions for future work. An Appendix is also included to characterize the continuum approach we have adopted, and some related scripts we developed for ABAQUS (i.e. the software on which the original LHHM is implemented).

2. Literature Review

2.1 Overview of Cardiac System

The cardiovascular system is the primary system responsible for maintaining a constant blood supply across tissue throughout the body. The heart is composed of four primary interconnected chambers (Fig. 1 a), namely the right and left atria, and the right and left ventricles. A healthy heart operates to receive deoxygenated blood from all tissue, deliver it to the pulmonary system for reoxygenation, and to subsequently deliver that reoxygenated blood to the rest of the body and itself. An electrical impulse triggers the active contraction of these chambers. The resulting pressure forces the blood from the right chambers up to the pulmonary system, and the blood in the left chambers down to the rest of the body. Thus, before completing one circulation of the body, blood must visit the heart twice. The four chambers are composed primarily of multinucleated cells, called cardiomyocytes, which handle the active mechanical response of the cardiac cycle (i.e., are responsive to the electrical stimulus). Meanwhile, valves and chordae located at the intersections of these chambers are more dominantly composed of fibrous extracellular proteins that passively handle both the mechanical and hydrostatic loads of the cardiac cycle, ensuring unidirectional flow into and out of their respective chambers

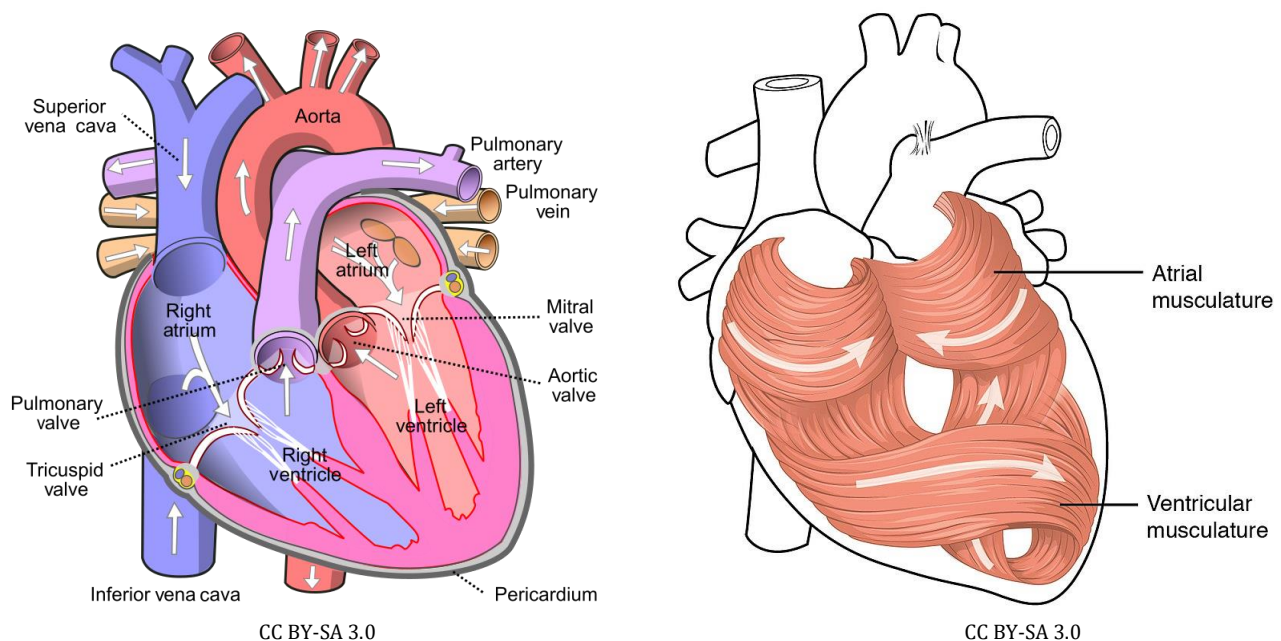


Figure 1 A diagram illustrating (Left) The major chambers and vasculature of the heart and (Right) the underlying musculature of the heart

The heart is enveloped in a fibrous sac called the pericardium. This envelop is fused to the diaphragm, thereby coupling heart motion to the breathing cycle as well. The outer surface of the heart is called the epicardium which remains in contact with the coronary system. The inner surface, called the endocardium, has direct contact with the circulated blood. The ventricles and atria are fused at a location named the annulus fibrosus, and this site is the location of the four coplanar valves. The Tricuspid valve (TV) allows blood to enter from the right atrium (RA) into the right ventricle (RV). It is a three-leaflet valve connected at the edge of its cusps to the papillary muscles (PM) of the RV via multiple tendons called the Chordae Tendineae. The Mitral valve (MV) functions similarly: separating the left atrium (LA) and the ventricle. The main difference between the MV and TV is that the MV is composed of only two leaflets, which are smaller in dimension than TV leaflets. On the other hand, the aortic and pulmonary valves both have three leaflets and no chordae, connecting the left ventricle to the aorta and pulmonary artery respectively. The musculature of the heart, first dissected and demonstrated by Francisco Torrent-Guasp, in which the ventricular muscles (called the ventricular band) descends from the base of the heart to the apex in the shape of a right-handed helix (Fig.1 b)(Buckberg et al., 2001). The fiber orientation relative to the plane of the short axis, varies transmurally (from endocardium to epicardium). Initially at an angle of -60° at the endocardium, and smoothly increasing to $+60^{\circ}$ at the epicardium (Streeter et al., 1969). Due to this unique architecture, the contraction of the heart creates a clockwise apical twist.

On a cellular level, the heart has a diverse range of specialized cells. Of relevance to this work are the main actors of the cardiac cycle: pace maker cells, conduction cells, and cardiomyocytes. Pace maker cells reside in two locations, the first of which is the sinoatrial node (SA), a group of cells at the lateral segment of the RA that have an unstable potential which depolarizes to trigger the heart-beat. The second is the atrioventricular node, a group of cells located at the site of atrial and ventricular fusion. This set of nodes also has an internal rhythm but conducts signals at a much slower speed (0.01 - 0.05 m/s) than other cardiac cells. The bundle of His transmits electrical impulses from the atrioventricular node to the ventricles of the heart. The bundle branches and divides into thin highly conductive wire-like cells called Purkinje fibers, that distribute the electrical impulse across the

ventricular muscle most quickly (3-5 m/s). They are situated along the endocardial layer of the ventricles. The bundle of His stems from the AV node and the Purkinje fibers travel down the septum to the apex of the heart, branching from there upward along the major walls of the chamber like fractals (Fig. 2 a). Myofibers, which are the predominant constituents of the chamber walls, conduct electrical signals at a more moderate speed (0.5-1 m/s) across the ventricles and the atria. All the cells we have here described can be collectively termed as cardiomyocytes (Widmaier, Raff, Strang and Vander, 2011).

Electrical conduction through cardiac fibers (myofibers) occurs with a synchronous triggering of ion exchange across cell membranes. This is a five-stage process in all cells except the SA cell (which exhibits a three-step process) (Fig. 2 b). The resting potential of ventricular and atrial cells is approximately -80 mV (stage 4) at which a greater concentration of potassium (K^+) ions remains inside the cell, while sodium ions (Na^+), calcium ions (Ca^{2+}) and chlorine ions (Cl^-) remain outside the cell. Once depolarized, Na^+ ions enter into the cell, rapidly increasing its potential to 20 mV in the process (stage 0). The closure of Na^+ membrane channels prohibits entry of further ions, while K^+ ions exit the cell, which brings the potential down to 0 mV (stage 1). Stages 0 and 1 take place over an infinitesimal time interval. Ca^{2+} also rushes into the cell causing an equilibrium with the outgoing K^+ of for approximately $0.2-0.4$ ms (stage 2). Finally, the ions are actively transported in and out via an ATP (Adenosine Triphosphate) driven Na^+-Ca^{2+} membrane

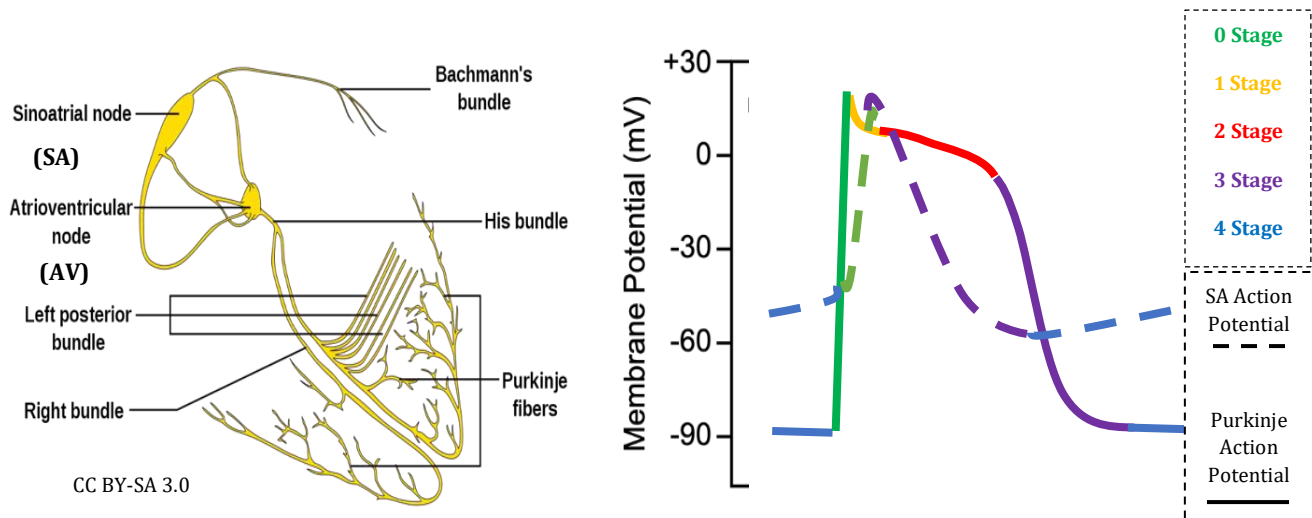


Figure 2 A schematic (Left) showing the underlying pacemaker cells and Purkinje Fibers as well as the major components of the conduction system. (Right) graph of potential in one beat.

channels to restore the resting potential of -80mV within 0.2-0.4 ms (stage 3). As heart muscle consists of many fibers connected in series by intercalated discs (membranous disks with surface proteins to relay the signal), and in parallel by collagen, signal conduction across the cardiac domain occurs primarily along primary fiber axes. The SA node often has a resting potential of -60 mV and is triggered at -50 mV due to fluctuating ion concentrations. While all cells have an inherent rhythm and can act as pace maker cells in times of distress (like ventricular tachycardia or ventricular arrhythmia)(Hampton and Hampton, 1998), the SA node generally generates a higher potential owing to its synchronized conduction in stage 0, and the inability of other cells to depolarize (termed refractoriness) in stages 1,2 and 3 with the closure of Na⁺ channels (Widmaier, Raff, Strang and Vander, 2011).

Myofibers are themselves striated, meaning that they are composed of fibers of structural proteins, called myofibrils. Myofibrils are bundled in sarcomeres which are placed in series along myofiber direction, in parallel with the mitochondria which are also oriented along fiber direction. A sarcomere is fused to its neighboring sarcomere at a site called the Z site, and at the midway between Z sites is a site termed A site, where the contraction occurs. Two major molecules are required to trigger contraction: Ca²⁺ and ATP. The flow of Ca²⁺ has been described above. ATP is gained as a product of cellular respiration. Ca²⁺ binds to tropomyosin, a protein that is sterically bound to the actin filament and myosin filament simultaneously. With its binding, tropomyosin releases the actin and myosin, allowing them to bind at the sites previously occupied by tropomyosin. This binding has a high affinity, so the myosin is hydrolyzed, releasing ADP (Adenosine diphosphate) and P molecules, and structurally changing as a result, pulling axially the Z actin filaments rooted at the Z sites. Shortening of the sarcomere thus results, i.e. muscular contraction at the cellular level. ATP then binds to myosin, lowering its affinity to actin. If tropomyosin is still bound to Ca²⁺, contraction occurs again. If Ca²⁺ is dissociated from tropomyosin (if intercellular Ca²⁺ concentration has been reduced) then tropomyosin will rebind to actin and myosin, inhibiting any further contraction. Control of intercellular Ca²⁺ concentration and myofibril sensitivity to Ca²⁺ determines cell contractility (Fig. 3). In a healthy heart beat, the resulting Active Force vs. Ca²⁺ concentration curve is S-shaped, with minimum force arising at 10⁻⁸ M of Ca²⁺ and maximum force arising at 10⁻⁶-10⁻⁵ M of Ca²⁺ (Shiels and White, 2008).

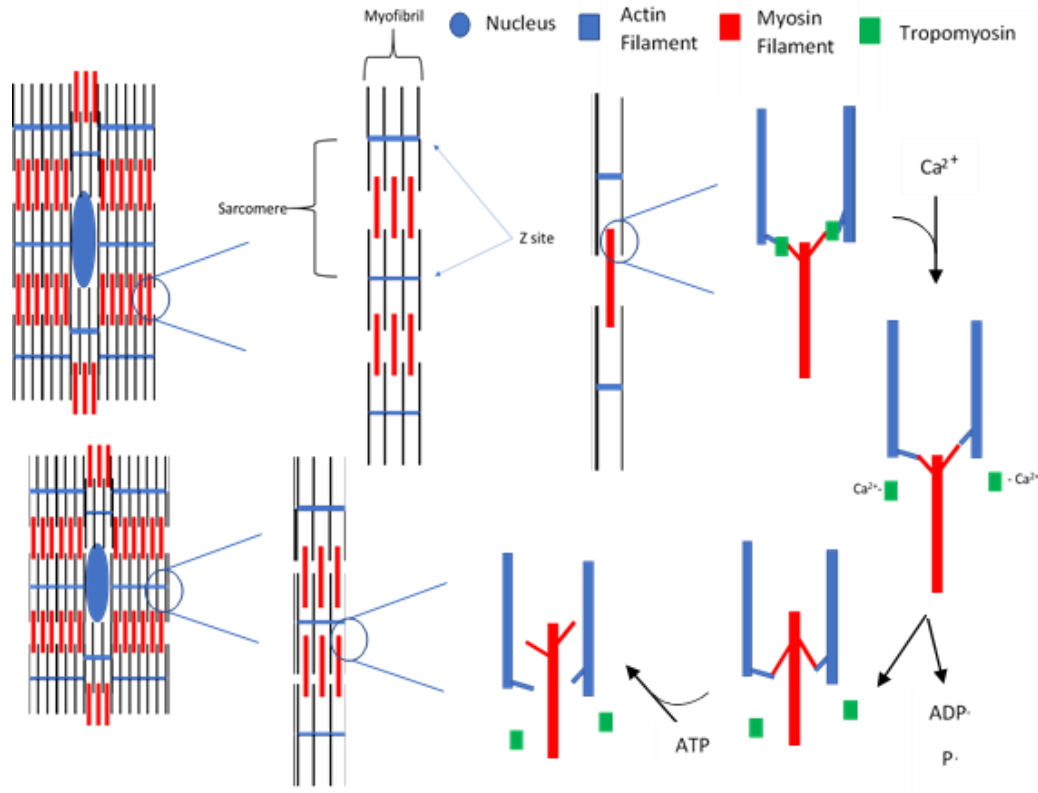


Figure 3 A schematic of striated myofibers and the process of contraction. The influx of Calcium ions during depolarization allows for unbinding of the actin-troponin-myosin complex, and phosphorylation of the actin-myosin complex causes contraction

A moderate increase in myofiber length associated with excessive blood pressures in ischemic myocardia is also associated with an increase in Ca²⁺ sensitivity with a maintained and contractile force. This is termed the Frank-Starling Effect (Fig. 4) (Shiels and White, 2008).

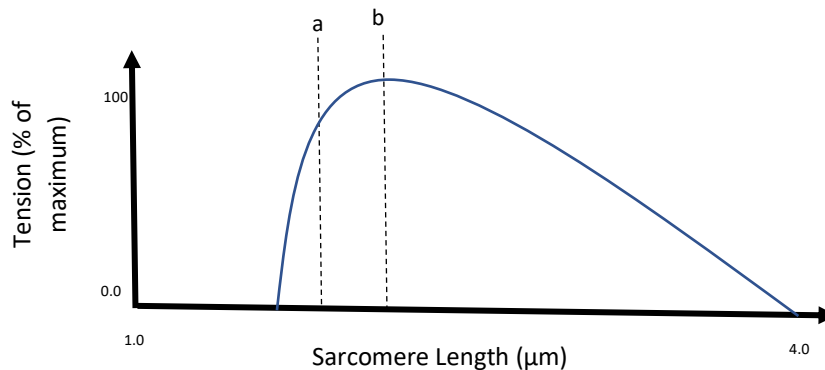


Figure 4 The Frank-Starling Effect shows the range of length at which active myofiber forces can be created. The length between a and b is optimum due to a large overlap between actin and myosin fibers, which maintains and increases contractility. Adapted from (Shiels and White, 2008)

The resulting mechanical cardiac cycle is thus composed of two major phases prescribed by the larger chambers: ventricular systole and ventricular diastole.

Ventricular systole describes the contraction of the muscle fibers, and the characteristic “lub-dub” sound of the heart marks its beginning and its end. This phase lasts for approximately 0.35s, evolving in two steps. The first step lasts for 0.05s and begins with the closure of the main valves (MV and TV), which makes the “lub” sound. All chambers contract while the volume of blood enclosed remains the same, therefore terming it isovolumetric contraction. LV pressure correspondingly climbs in healthy adults from 10 mmHg to approximately 80 mmHg, bringing about the next phase, which begins with the AV and PV opening and ventricular blood ejection occurs. In this step, aptly termed ventricular contraction, the systemic pressure increases to 120 mmHg in healthy adults, and pulmonary pressure reaches 25 mmHg. This step lasts for approximately 0.3s and is concluded by the closing of the AV and PV (making a fainter “dub” sound). A healthy Ejection Fraction (EF), which is defined as a percentage of blood ejected from the LV, is approximately 58%. The next phase of the cardiac cycle is the relaxation phase or diastole. It again begins with isovolumic relaxation with myofibers returning to their original length. LV pressure here decreases once again to 10 mmHg and the final stage in the cardiac cycle is of ventricular diastole, or (filling), where the MV and TV open and blood flows into the cardiac chambers.

Table 1 Breakdown of the Cardiac Cycle

		Duration (seconds)	MV/TV State	AV/PV State	Ventricular Pressure	Ventricular Volume
<i>Systole</i>	Isovolumetric Contraction	0.05	Closed	Closed	Increasing	Constant
	Ventricular Contraction	0.3	Closed	Open	Increases to peak then decreases	Decreasing
<i>Diastole</i>	Isovolumetric Relaxation	0.08	Closed	Closed	Decreasing	Constant
	Ventricular Filing	0.45	Open	Closed	Almost fixed	Increasing

The next phase of the cardiac cycle is the relaxation phase or diastole. It again begins with isovolumic relaxation with myofibers returning to their original length. LV pressure here decreases once again to 10 mmHg and the final stage in the cardiac cycle is of ventricular diastole, or (filling), where the MV and TV open and blood flows into the cardiac chambers. Table 1 summarizes the steps of the cardiac cycle and the state of the valves throughout it (Feher, 2016).

It is important here to note that Atrial systole begins approximately 0.15 seconds before ventricular systole begins, in order for blood to be moved into the ventricles from the atria. This happens largely thanks to the delay induced by the AV node, allowing the atria to push blood into the ventricles for improved filling (Feher, 2016).

End Systolic Volume (ESV) and End Diastolic Volume (EDV) are both factors that determine the Stroke Volume (SV), i.e. the amount of blood ejected from the LV during systole. The Frank-Starling Effect dictates that at the optimum length, an increase in overload will be associated with an increase in SV. If the afterload causes excessive sarcomere lengthening (ventricle dilation), cardiac output will decrease and the heart will begin hypertrophy. The SV is computed as $SV = EDV - ESV$, and the corresponding Ejection Fraction is given as $EF = \frac{SV}{EDV}$. Finally, Cardiac Output (CO) is calculated from the Heart Rate (HR) and the SV as $CO = HR \times SV$. Cardiac output is an important clinical indicator of healthy ventricular function, and represents the flow rate of oxygenated blood into the body (Fig 5.).

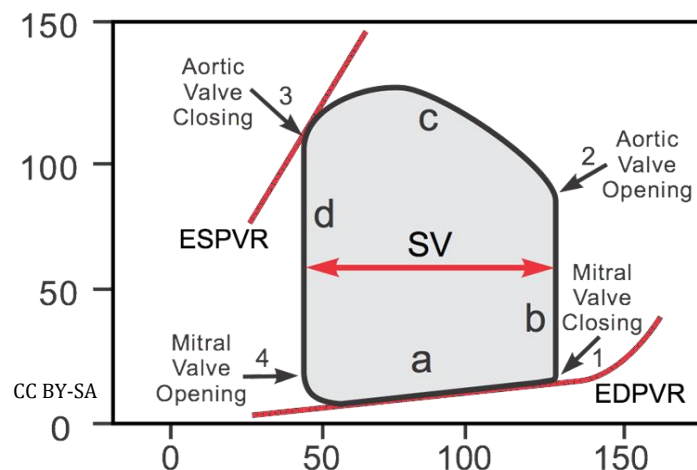


Figure 5 Example of Pressure-Volume Loop and their corresponding place in the cardiac cycle

2.2 Pathologies of Interest

2.2.1 Pulmonary Hypertension

Pulmonary hypertension (PH) has long been a pathology of interest to the study of RV remodeling mechanisms and, consequently, patterns of adaptation and maladaptation under various straining conditions (Shapiro, Nishimura, McGoon and Redfield, 2006). The RV is characterized by a crescent-shape, constituted of thin walls of higher compliance, and exhibiting a lower pressure state. It shares the interventricular septum (IVS) with the LV and, by virtue of its curvature, it appears as wrapped around the LV, allowing for interventricular dependence (Giusca, Jurcut, Gingham and Voigt, 2010; Chin and Coghlan, 2012). Pulmonary hypertension, as per the 6th World Symposium on Pulmonary Hypertension, is defined as an elevation of the mean pulmonary arterial pressure (mPAP) to 20 mmHg (Hoeper and Humbert, 2019). Under normal circumstances, the RV functions in a low-pressure system and tolerates only small variations in afterload. Upon chronic exposure to elevated pressures, a resultant adaptive response leads to myocardial hypertrophy and subsequent contractile dysfunction (Jurcut et al., 2011; Naeije and Dedobbeleer, 2013). Although not fully understood, these changes at the molecular level have been thought to be secondary to, among others, decreased contractility, cardiomyocyte apoptosis, and fibrosis (van de Veerdonk, Bogaard and Voelkel, 2016).

The World Health Organization (WHO) classifies pulmonary hypertension into five groups according to their underlying mechanism. While pulmonary arterial hypertension results from an alteration in the vasculature exclusively affecting the pulmonary circulation, secondary pulmonary hypertension is characterized by an underlying etiology leading to hypoxic vasoconstriction and subsequent remodeling of the pulmonary artery vasculature (Fox and Khattar, 2006; McLaughlin et al., 2009). Such etiologies include left heart disease, lung conditions, thromboembolic diseases, etc.

Although rare, early detection can allow for surgical intervention and prevention of irreversible RV remodeling, unlike in most causes of PH (Humbert, 2010; Delcroix et al., 2012). The distinction between subclasses of PH is critical, as different biological mechanisms of pulmonary changes lead to different types of RV remodeling and clinical prognostication. Echocardiography is the usual primary diagnostic tool to assess cardiac

function and to exclude secondary causes of RV failure. For instance, Tricuspid annular plane systolic excursion (TAPSE) is a scoring system used with Doppler to determine RV function by assessing apex-to-base shortening of myocardial fibers (Ueti et al., 2002). It quantitatively measures the displacement of the lateral tricuspid annulus toward the apex during systole. It is a rapid and reproducible parameter that correlates with RV ejection fraction (RVEF) to a high degree (Kaul, Tei, Hopkins and Shah, 1984). TAPSE has been shown to be effective in assessing global RV function in myocardial infarction, pulmonary hypertension, and in patients with pulmonary embolism undergoing pulmonary embolectomy (Samad, Alam and Jensen-Urstad, 2002; Bashline and Simon, 2019).

To understand progression of PH disease, quantitative prediction of RV strain states and remodeling is paramount. The prediction of RV dysfunction evolution towards severe RV failure, and its irreversible structural changes, requires the numerical methods of biomechanics. Such methods promise an ability to determine clinically the critical point at which irreversible changes to the myocardium would necessitate surgical intervention.

2.2.2 Functional Tricuspid Regurgitation

Valvular anatomy is markedly different from ventricular and atrial anatomy, largely due to the non-contracting role of the valves. The tricuspid annulus (TA) is a distinct, saddle-shaped (Knio et al., 2016) ring, see Figure 6, that acts as a morpho-elastic region of transition connecting the ventricle to the TV leaflets, with a typical ES diameter of 31.5 mm in healthy individuals (Dwivedi et al., 2014). The tissue of the annulus is constituted from two phases, with the first consisting of two intermeshed orthogonal myofibrils aligned circumferentially and radially to the valve. The second phase is a collagen-based segment that contains few myofibrils at the anterior and posterior leaflets, with none at the septal leaflet.

TV leaflet cellular anatomy is mostly fibrous, consisting of valvular interstitial cells, that create structural proteins of the tissue, and no cardiomyocytes or myofibrils. The fibrous constituents play different roles, with elastin and collagen playing the major role in elastic load bearing, while water-infused proteoglycans (PGs) and glycoaminoglycans (GAGs) acts as damping (Eckert et al., 2013). The lamina facing the atria and ventricles consist largely of elastin-collagen dense protein, while the main thickness of the leaflets consists of PG and GAG dense lamina, with major fibers oriented circumferentially and radially. The elasticity

of TV leaflets is associated with many diseases, and of particular importance to our discussion is TA dimensions, which indicate functional efficiency of valve closure and coaptation.

Mitral Valve Regurgitation (MR) is a valvular disease affecting approximately 0.59% of adults worldwide. Its prevalence increases significantly with age (Dziadzko and Enriquez-Sarano, 2016). MR is associated with LV dysfunction, is characterized by incomplete MV leaflet coaptation and in severe cases leads to Heart Failure (HF). It is also a major factor in the onset of Pulmonary Hypertension (PH), creating a higher RV afterload, ultimately causing RV dilation and secondary Tricuspid Valve Regurgitation (TR) (Badano, Muraru and Enriquez-Sarano, 2013). This condition is also termed Functional TR (FTR), and occurs in approximately 30% to 50% of those with severe MR (Cohen, Sell, McIntosh and Clark, 1987; Koelling et al., 2002) with incidences of severe FTR in approximately 14% of patients who underwent MV replacement (Izumi, Iga and Konishi, 2002). It is largely agreed upon that FTR is primarily described by TA dilation and flattening (Ton-Nu et al., 2006) with a loss in annulus saddle shape, and with annulus diameter exceeding 40 mm, see Fig. 6 (Nishimura et al., 2014).

While common for patients with severe MR to undergo MV replacement surgery, assessment of FTR and agreement on intervention and its necessity, in the form of TV annuloplasty varies among experts in the cardiologist community (David, David and Manhiolt, 2015; Shuhaiber, 2018), with many drafting different guidelines to help classify patients and their respective intervention policies. Dreyfus et al. give focus to the TA diameter and the degree/location of leaflet coaptation, recommending ring annuloplasty for dilated TAs and edge-to-edge (instead of belly-to-belly) leaflet coaptation (Dreyfus et al., 2015). Others recommend intervention based on presence of other diseases like PH and if another heart-surgery is already taking place (Verdonk et al., 2018).

Many procedures regarding repair of the TV exist, including the suturing of two TV leaflets at the middle of their edges called the “clover” technique (Belluschi et al., 2018), and recently the adaptation of an intervention previously used to treat regurgitant MV leaflets by pinching them together using a device named MitralClip (Dabiri et al., 2019) . On other

hand, the De Vega technique involves the suture of components of the TA (Wei, Chang, Lee and Lai, 1993), and the use of annuloplasty rings, first employed by Carpentier et al. (Carpentier et al., 1971), has become a popular choice for valve repair. Both rigid and semi-rigid rings can be used and the choice between them will determine the amount of TA remodeling, although care must be given to the cardiac tissue's ability to withstand the large cyclical forces (Pfanmüller et al., 2012).

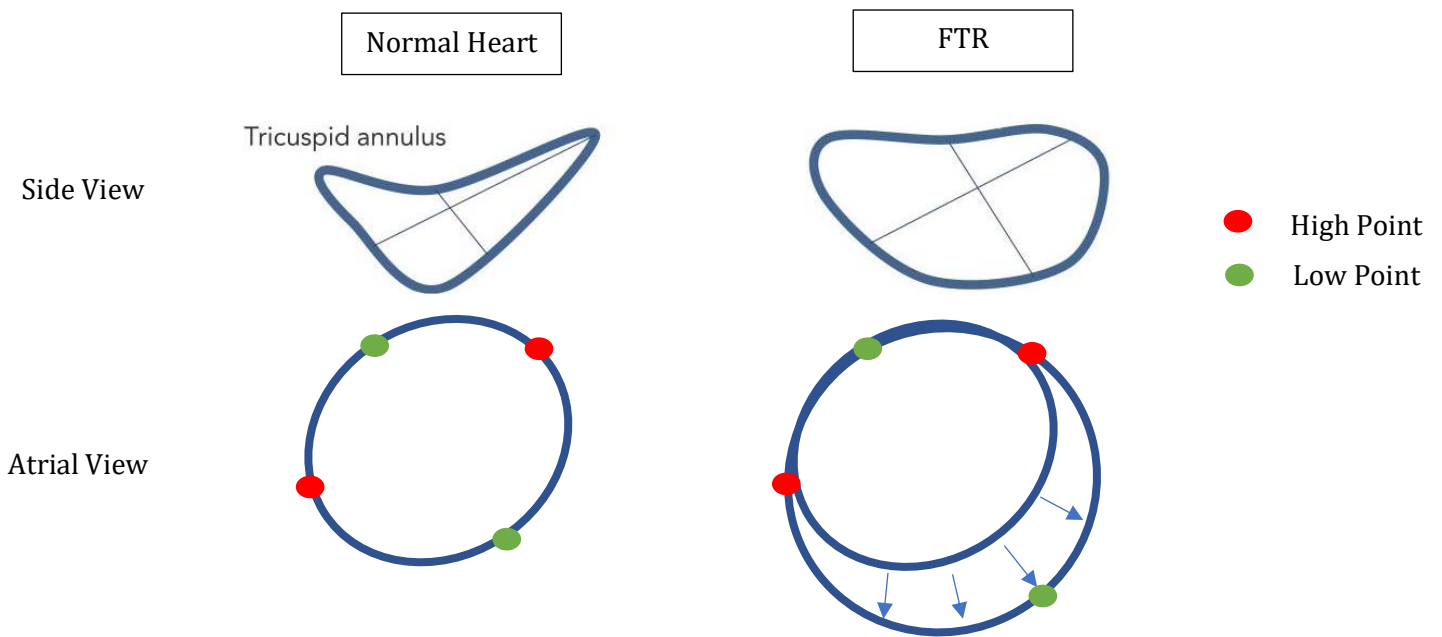


Figure 6 The saddle shape associated with a healthy TA is made more flattened and circular. Right side failure often associated with RA and RV dilation causes an increase in annulus size in the lateral direction. Adapted from (Bessler, Meduli and Lurz, 2017)

2.3 Computational Assessment of Pulmonary Hypertension and Regurgitant Valves

We here address existing work dedicated to the assessment of Pulmonary Hypertension and Functional TR. Since most of these works include constitutive modelling, a brief overview of continuum mechanics is appended to this thesis.

2.3.1 Pulmonary Hypertension

While little attention is given to RV research in general, there is a large gap in computational work targeting RV failure especially in the context of PH. With a wide array of pathophysiologies associated with PH, different research has chosen to focus on capturing different aspects of the disease. We here highlight the growing interest in capturing the remodeling associated with PH, as well as the studies associated with afterload generation and its effect on cardiac function.

A fundamental contribution to the simulation of growth of cardiac tissue came from (Göktepe, Abilez, Parker and Kuhl, 2010), in which they outline two methods of sarcomeric growth. Both strain-dependent growth (which describes ventricular dilation) and stress-dependent growth (which describes ventricular thickening) are described by the multiplicative decomposition of the deformation gradient into an elastic and growth parts:

$$\mathbf{F} = \mathbf{F}_{elastic} \cdot \mathbf{F}_{Growth}, \quad \text{Equation 1}$$

In the case of strain-dependent growth, a multiplier $g(\lambda)$ is introduced where

$$\mathbf{F}_{Growth} = \mathbf{I} + (1 - g(\lambda))\mathbf{f}_0 \otimes \mathbf{f}_0, \quad \text{Equation 2}$$

Where \mathbf{I} is the identity matrix and \mathbf{f}_0 is the unit vector in the fiber direction. The growth multiplier g is dependent on strain per the form below:

$$\begin{aligned} \frac{dg}{dt} &= K(g)\varphi(\lambda), \\ K(g) &= \frac{1}{t_0} \left(\frac{g_{max} - g}{g_{max} - 1} \right)^\gamma, \\ \varphi(\lambda) &= \frac{\lambda}{g} - \lambda_{threshold}, \end{aligned} \quad \text{Equation 3}$$

Where g_{max} is the maximum possible fiber stretch, t_0 is the time it takes to stretch the fiber, γ describes nonlinear stretch dependence in the direction of fibers, and $\lambda_{threshold}$ is the stretch beyond which growth will develop. A similar formulation is adopted for stress-

dependent growth, but fibers expand circumferentially along the direction of the sheet (\mathbf{s}_0) instead of the fiber as follows:

$$\begin{aligned}\mathbf{F}_{Growth} &= \mathbf{I} + (1 - g(\text{tr}(\boldsymbol{\sigma})))\mathbf{s}_0 \otimes \mathbf{s}_0, \\ \frac{dg}{dt} &= K(g)\varphi(\text{tr}(\boldsymbol{\sigma})), \\ K(g) &= \frac{1}{t_0} \left(\frac{g_{max}-g}{g_{max}-1} \right)^\gamma, \\ \varphi(\lambda) &= \text{tr}(\boldsymbol{\sigma}) - p_{th},\end{aligned}\tag{Equation 4}$$

Where $\boldsymbol{\sigma}$, is the Cauchy stress and p_{th} is the pressure applied on-sheet beyond which it will grow. (Rausch et al., 2010) revisited this formulation, integrating it with a constitutive model of passive stress developed by (Holzapfel and Ogden, 2009) and an active stress developed by (Guccione et al. 2001). They applied a constant pressure on a biventricular geometry to represent increased afterload due to pulmonary hypertension, and they demonstrated RV wall hypertrophy until RV and fluid pressure come to equilibrium. No attempt was however made to address patient-specific geometries; nevertheless, recent work by (Avazmohammadi et al., 2019) adopted the strain-dependent growth method to model induced PH in an experimental setup involving rat hearts. A biventricular model was segmented from a non-PH rat, and a hyperelastic formulation based on (Guccione, McCulloch and Waldman, 1991) incorporating a Fung-type model was used:

$$\Psi_{deviatoric} = \frac{c}{2} \left(e^{b[B_1 E_{ff}^2 + B_2 (E_{ss}^2 + E_{nn}^2 + 2E_{sn}^2) + B_3 (E_{fs}^2 + E_{fn}^2)]} - 1 \right), \tag{Equation 5}$$

where c , b , B_1 , B_2 and B_3 are material constants. E_{11} is the Green-Lagrange strain component along the fiber direction, and E_{22} and E_{33} represent strain along the sheet and normal directions, respectively. They based their active stress component on (Hunter, McCulloch and Keurs, 1998), which is given by

$$T_{active} = \frac{T_{Ca^{2+}}}{2E_{ff}+1} [1 + \beta(\sqrt{2E_{ff} + 1} - 1)]\mathbf{f}_0 \otimes \mathbf{f}_0, \tag{Equation 6}$$

Where $T_{Ca^{2+}}$ defines the force generated by the myofibers at a given calcium ion concentration, and β is a material constant. Their formulation was used to successfully study

the progression of PH and RV remodeling at different time-points. While showing promise as a tool to model RV growth and remodeling, their study presents with some clear limitations that relate to their lack of comparison to cardiac output and function against clinical markers.

A patient specific adaptation of growth came in (Finsberg et al., 2019), who recently modified the methods outlined above, and applied them on a patient's biventricular model. In particular, they redefine:

$$\mathbf{F}_{Growth} = \frac{1}{\sqrt{1-g}}(\mathbf{I} - \mathbf{f}_0 \otimes \mathbf{f}_0) + (1 - g)\mathbf{f}_0 \otimes \mathbf{f}_0, \quad \text{Equation 7}$$

where g is a patient specific parameter. Their passive response is governed by a transversely isotropic form of (Holzapfel and Ogden, 2009):

$$\Psi_{deviatoric} = \frac{a}{2b}e^{b(I_1-3)} + \frac{a_f}{2b_f}(e^{b_f(I_{4f}-1)^2} - 1), \quad \text{Equation 8}$$

Where a , b , a_f and b_f are material constants. Optimization of stiffness a and growth parameter g was made for heart geometries to correctly correspond to patient parameters of cardiac output as obtained from 17 patients (5 normal and 12 hypertensive). No clear account was given of how the active stresses were applied. The full cardiac cycle was modelled and they concluded that RVEDV/LVEDV is a strong predictor for determining PH, as well as a pronounced increase in longitudinal strain exhibited in models of PH.

As mentioned earlier, the different pathophysiologies of PH have different impacts on the cardiac muscle and the body as a whole. (Kheyfets et al., 2013) highlights the use of CFD to investigate change in pulmonary circulation on patient-specific MRI images of the pulmonary system instead of the heart. A less computationally aggressive approach was adopted by (Lungu et al., 2016), who have used 0D and 1D Windkessel models to investigate wave reflections caused by increased afterloads. They opted to forgo the modelling of the cardiac tissue, and instead use segmented MRI images of patient ventricles to define boundary conditions in their fluid models. The impact of PH on RV and septal curvature of 30 patients (10 normal and 20 hypertensive) was also assessed by (Palumbo et al., 2018), which revealed a direct correlation between curvature and mPAP, with septal curvature changing from negative to positive in PH (in septum EDV, $R=0.73$, at ESV, $R=0.82$).

Another study by (Xi et al., 2016) also investigated changes in septum curvature in PAH, this time in a full simulation of a beat instead of just using MRI images. Their study appears to be the only to attempt electromechanical coupling of the biventricular model and a simple voltage and strain dependent diffusion equation. A 0D Windkessel model is used to model systemic and pulmonary pressures, and a Fung-type constitutive model for passive tissue response is used as shown below:

$$\Psi_{deviatoric} = \frac{c}{2} \left(e^{[B_1 E_{ff}^2 + B_2 (E_{ss}^2 + E_{nn}^2 + E_{sn}^2 + E_{ns}^2) + B_3 (E_{fs}^2 + E_{sf}^2 + E_{fn}^2 + E_{nf}^2)]} - 1 \right), \text{Equation 9}$$

Where c , B_1 , B_2 and B_3 are material constants (E_{ij} , $i, j = \{f, s, n\}$) are components of the Green-Lagrange strain tensor. The active response used is a function of state variables s , stretch λ , rate of stretch $\frac{d\lambda}{dt}$, and a parameter of contractility T_{ref} . Unfortunately, no further explanation of was given, and no data regarding the material parameters of the Fung-type model were presented. Their findings include an increased LV longitudinal strain in PH compared to normal, as well as a flattening of the septum as concluded in (Palumbo et al., 2018).

We thus remark that the mechanisms by which growth is modeled have not been thoroughly verified, and that their dependence on time and strain alone does account for the physiological changes that occur during PH. Moreover, they do not account for physiological differences between, human and rat hearts. For instance, in humans, an elevated mPAP can lead to an increase in the number of collagen fibers in a cardiomyocyte (thus increasing stiffness of the fiber), but a decrease in collagen interconnectivity (Liu and Wang, 2019). The strain independent maximum force generated during contraction (incorporated as a constant called contractility in most models) plays a direct impact on PH (Pewowaruk et al., 2018). Taking this into account in constitutive models is not trivial, and the role of cellular activity and oxidative stress resulting from PH on these models remains unclear.

2.3.2 Functional Tricuspid Regurgitation

Different approaches to capturing valve stress-strain behavior have been adopted; however, general consensus is to model TV leaflets as hyperelastic, with two families of fibers (Lee et al., 2019). For instance, a study by Aversa et al. adopted equibiaxial data for human TV leaflets from Pham et al., and used a strain energy function (SEF) defined by Lee et al. to govern TV leaflet response (Lee et al., 2013; Aversa and Careddu, 2017; Pham et al., 2017).

$$\Psi_{deviatoric} = C_{10}(I_1 - 3) + \frac{c_0}{2} [(1 - \beta)e^{c_1(I_1-3)^2} + \beta e^{c_2(I_4-1)^2} - 1], \quad \text{Equation 10}$$

(Kong et al., 2018) use the same data with a different SEF, described by (Holzapfel, Gasser and Ogden, 2000) as,

$$\Psi_{deviatoric} = C_{10}(e^{c_{01}(I_1-3)} - 1) + \frac{k_1}{2k_2} \sum_{i=c,r} [e^{k_2(\kappa I_1 + (1-3\kappa)I_{4i}-1)^2} - 1], \quad \text{Equation 11}$$

In Equations 10 and 11 above C_{10}, C_{01} , are material constants that describe the isotropic response in the first term of the SEF. c_1, c_2, k_1 and k_2 are the remaining material constants describing the orthotropic terms. In Equation 10, β is a value between 0 and 1 and represents anisotropy, while in Equation 11 κ is a value between 0 and 1/3 and is also used to represent anisotropy. The term I_1 is the first invariant of the right Cauchy-Green tensor and is given by $I_1 = \text{trace}(\mathbf{C})$. The fourth invariants of \mathbf{C} , I_{4C} (Circumferential) or I_{4R} (Radial) can be evaluated as $I_{4i} = \mathbf{i} \cdot (\mathbf{C}\mathbf{i})$ where \mathbf{i} is the direction vector.

A comment must here be made about these two models. Despite accounting for the orthotropic response, they assume that the two fibers in the model have the same fundamental response as each orthotropic term has the same constants and only differs in the invariant. The models also use the same term to represent the isotropic response in $C_{10}(e^{c_{01}(I_1-3)} - 1)$, and anisotropy is accounted for through only a constant in the model (β or κ). This is largely due to the fact that equibiaxial data was used and no data including shear was used (Lee et al. 2019).

Finally, a study by (Khoiy and Amini, 2016) fitted their Fung-type model to biaxial data with five pairs of stretch ratios, and present the most extensive data reported yet,

$$\Psi_{deviatoric} = \frac{c}{2} \left(e^{[a_1 E_{CC}^2 + a_2 E_{CC}^2 + 2a_3 E_{CC} E_{RR}] - 1} \right), \quad \text{Equation 12}$$

where c , a_1 , a_2 and a_3 are material constants. The parameters E_{CC} and E_{RR} represent the Green-Lagrange strains in the circumferential and radial directions, and a_3 is the term representing anisotropy. They then tested this model on data with pure shear and their model predicted stress correctly when compared to experimental data. While to date these represent a rigorous study of constitutive modelling of the TV, there is a clear disparity between a focus on constitutive modeling and investigative studying of MV and AV responses as compared to TV behavior; as such, more effort to bridge this gap appeared in order.

With recent growth in computational tools, attention has been indeed given to creating comprehensive computational models of the heart that reflect anatomical and physiological diseases to lend insight into relevant pathophysiology, complications and intervention policies. For example, recent work highlighting the effect of annuloplasty on regurgitant MV has been presented (Baillargeon et al., 2015). More recent work focusing on Finite element TV modeling captured patient-specific dynamics of healthy TV geometry, as obtained from Multi-sliced computer tomography (MSCT) (Kong et al., 2018). A subsequent analysis by (Singh-Gryzbon et al., 2019), addressed some of the assumptions made in (Kong et al., 2018) by setting up an experimental framework to capture TV and Chordae geometry, while employing Fluid-Structure Interaction (FSI) to computationally determine the effect of TR on hemodynamics. Most recently a (Dabiri et al., 2019) have used FSI to demonstrate the application of MitralClip, and its ability to reduce regurgitation in the TV.

The previous work (shown in Table 2) establishes a strong basis for computational analysis of TV diseases; however, in the case of FTR where the disease is dictated by the geometry of the TA during the cardiac cycle, these works fall short of an accurate description. In the case of (Singh-Gryzbon et al., 2019), the TA is fixed altogether, and the regurgitation is induced from chordal and papillary muscle placement. In (Dabiri et al., 2019) the TA, chordae and PM are attached to the walls of a cylindrical elastic tube in the short-axis of the TV, while in (Kong et al., 2018) the TA motion is assumed to be uniform, while the location of the chordae are iteratively adjusted and the PM location is approximated. For this reason,

we see a clear need to highlight the influence of the ventricles and TA dynamics on valve dynamics, especially in the study of diseases associated with TA defects such as FTR.

Table 2 Summary of Computational Modelling of FTR

Publication	Constitutive Model	Model Parameters	Boundary Conditions (TA)	Chordae Position	Fluid Model
(Aversa and Careddu, 2017)	(Lee et al., 2013)	Equibiaxial data from (Pham et al., 2017)	Fixed TA	Fixed PM	Load applied on Ventricular side
(Baillargeon et al., 2015).	(Holzapfel and Ogden, 2009)	Biaxial Data from (Kunzelman and Cochran, 1990)	Attached to RV	Iteratively Adjusted Until Valve Closed	Load Applied to Ventricular Side
(Kong et al., 2018).	(Holzapfel et al., 2000)	Equibiaxial data from (Pham et al., 2017)	Assumed	Iteratively Adjusted	Load Applied to Ventricular Side
(Khoiy and Amini, 2016)	Fung-Type	Experimentally Determined	-	-	-
(Singh-Gryzbon et al., 2019)	-	-	Fixed TA (According to experiment)	Imaged from Experimental Setup	FSI
(Dabiri et al., 2019)	(Holzapfel and Ogden, 2009)	(Kunzelman and Cochran, 1990)	Fixed to Elastic Tube	Fixed to Elastic Tube	FSI

2.4 The Living Human Heart Model

The Living Heart Project is an international research collaboration dedicated to the development of a computational platform for the assessment of cardio-pathologies *in silico*. The platform uses the commercial finite element (FE) software, Abaqus/CAE (SIMULIA, Providence, RI). Focus is given to the study of a few beats (three – five) of a full-heart Multiphysics (electro-mechano-physiological) model of a 25-year-old healthy male, called the Living Heart Human Model (LHHM). The LHHM includes the definition of a sequentially coupled electrical-mechanical analysis of a beat cycle with a one-second duration, which corresponds to a heart rate of 60 beats per minute, a typical adult (resting) heart rate. As such, it can be used to study the electrical behavior of the heart by itself or to examine its coupled electromechanical behavior wherein the mechanical response is driven by an electrical field.

2.4.1 Geometry and Framework

The LHHM is shown in Fig. 7 a. It includes well-defined anatomic details of the heart as well as proximal vasculature, such as the aortic arch, pulmonary artery, and superior vena cava (SVC).

The NURBS geometry of the modeled heart (at 70% ventricular diastole) comprises an assembly of individual parts. Most parts have been meshed by continuum solid tetrahedral elements -in the tissue- and are included in the typical analysis. Additional un-meshed parts are available, and can be incorporated in specific applications when needed. The LHHM further includes un-imaged chordae, bundle of His and Purkinje fibers with its imaged geometry, which was supplied by the *Zygote Media Group, Inc.*, though some of the parts in the LHHM were subsequently adjusted to enhance mesh discretization quality.

Representative geometries for the bundle of His and the Purkinje fibers were approximated on the endocardial surface of the right and left ventricles using fractal-trees, as described in (Sahli Costabal, Hurtado and Kuhl, 2016). The approximation itself builds on the method described in (Kotikanyadanam, Goktepe and Kuhl, 2010), where fibers are modeled as 1D electrical elements with a uniform conductivity that exhibit higher conduction velocities than the surrounding cardiac tissue. The Purkinje network is coupled to the myocardium at the terminus of the network branches. At the end of the network

branches, single 1D electrical conduction "resistor" elements are defined, and then the free end is tied to the myocardium. The resistors have the same uniform conduction properties as the ventricle. This methodology for Purkinje-myocardium coupling is described in (Bordas et al., 2012).

As for the atria and the ventricles, local myofiber orientations are defined as a Discrete Field on Abaqus/CAE. This methodology requires that a separate orientation be defined at the centroid of each element of the mesh. Fiber angle, α , in the ventricles is approximately equal to -60° on the epicardium and $+60^\circ$ on the endocardium, as shown by (Streeter et al., 1969), and consistent with (Genet et al., 2015). The fiber orientations in the atria (as well as the superior vena cava, aortic arch, and pulmonary trunk) were approximated using Figure 20 in the euHeart Final Project Report (euHeart, 2013). The model includes three Discrete Field definitions (named R_Atrium, L_Atrium, and Ventricles). For the Superior Vena Cava (SVC), aortic arch, and pulmonary trunk, local fiber orientations are defined using Part Geometry instead of a Discrete Field, since they are essentially tubular surfaces. For these regions, fiber normal direction corresponds to the geometric surface normal, and a geometric edge is used to define either the local sheet or fiber direction.

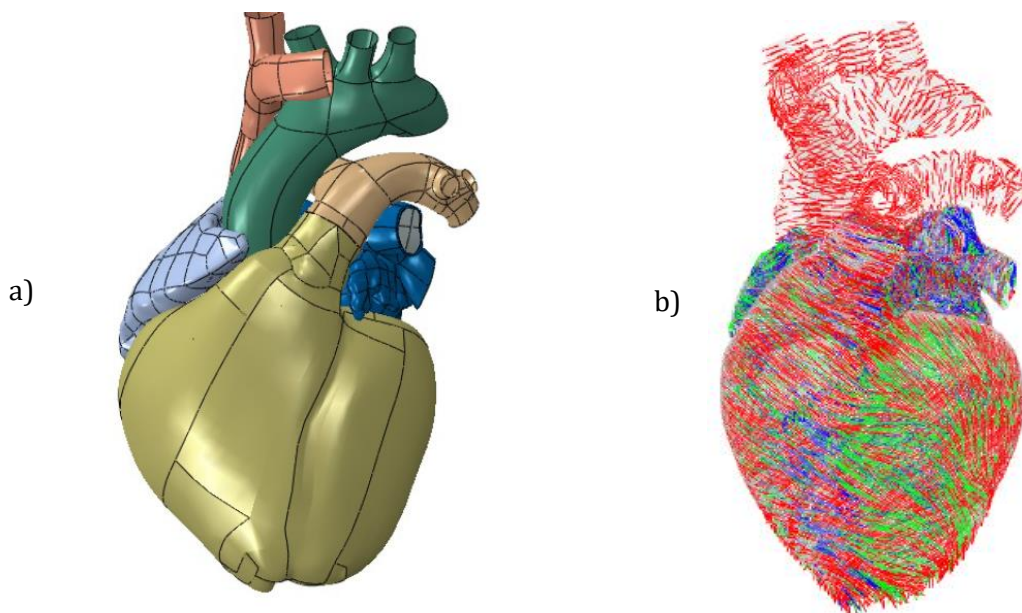


Figure 7 Geometry of 25-year-old healthy male heart used in LHHM (left). Superimposed Fiber Orientation (Right). Red - Epicardial Fiber. Green - Mid Myocardial Fibers. Blue - Endocardial Fibers

2.4.2 Electrical Modelling

Electrical (chemical species) conduction through cardiac tissue is triggered at the Sinoatrial (SA) node, and is modeled on the LHHM using the HETVAL subroutine, and the Abaqus Standard Implicit FE solver to simulate a single-beat for 500 ms, by implementing the monodomain reaction-diffusion model outlined in (Hurtado and Kuhl, 2012), and is given by:

$$\frac{d\phi}{dt} + \nabla \cdot (-\mathbf{D}\nabla\phi) = f(\phi, r), \quad \text{Equation 13}$$

Where ϕ is the transmembrane potential in millivolts, and \mathbf{D} is the (Eulerian) second order diffusion tensor defined by:

$$\mathbf{D} = d^{iso}\mathbf{I} + d^{ani}\mathbf{n} \otimes \mathbf{n}, \quad \text{Equation 14}$$

which can account for both isotropic diffusion d^{iso} and anisotropic diffusion d^{ani} along fiber direction \mathbf{n} . The source term $f(\phi, r)$ is defined by:

$$f(\phi, r) = c\phi(\phi - \alpha)(1 - \phi) - r\phi, \quad \text{Equation 15}$$

where c is a scaling parameter and α describes the oscillation threshold characterizing pacemakers and non-pacemaker cells. The recover term r defines local tissue restitution post-excitement, and is governed by:

$$\frac{dr}{dt} = \left(\gamma + r \frac{\mu_1}{\phi + \mu_2}\right)(-r - c\phi(\phi - b - 1)) \quad \text{Equation 16}$$

where γ represents a parameter directly proportional to the refractory period (Fig. 8), and b corresponds to a phenomenological parameter. The parameters μ_1 and μ_2 define the shape of the restitution curve. The voltage at an element is evaluated as $V = -80 + (100\phi)$ where ϕ ranges from 0 mV to 1 mV. The activation threshold of ϕ is 0.3 mV.

In the LHHM, conduction across the AV node is delayed by 85 ms before triggering the Purkinje fibers via the bundle of His, see Fig. 2.

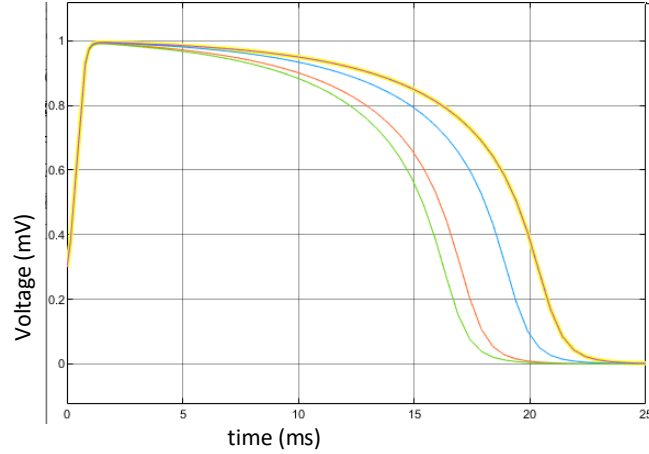


Figure 8 Implementation of Biochemical Model. Different graphs correspond to different refractoriness characteristic of tissue properties

2.4.3 Mechanical Modelling

Mechanical response of the cardiac tissue is implemented in the LHHM using an Abaqus Explicit FE solver, along with the VUANISOHYPER subroutine, which incorporates an active model that describes the contraction of the fibers due to electrical excitation, and a passive model that describes the non-excitable material behavior. The passive response was modeled after the incompressible, anisotropic, hyper-elastic model outlined in (Holzapfel and Ogden, 2009), given by the SEF:

$$\Psi_{deviatoric} = \frac{a}{2b} e^{b(I_1-3)} + \sum_{i=f,s} \frac{a_i}{2b_i} (e^{b_i(I_{4i}-1)^2} - 1) + \frac{a_{fs}}{2b_{fs}} (e^{b_{fs}(I_{8fs})^2} - 1), \text{ Equation 17a}$$

$$\Psi_{volumetric} = \frac{1}{D} \left(\frac{J^2-1}{2} - \ln(J) \right), \text{ Equation 17b}$$

where a, b, a_f, a_s, a_{fs} and b_{fs} are material constants. The value of I_1 describes the isotropic response and is the first principle invariant of the right Cauchy-Green tensor, \mathbf{C} , and is given by $I_1 = tr(\mathbf{C})$, while the two terms which describe the transversely isotropic response are described by I_{4f}, I_{4s} both evaluated as $\mathbf{f}_0 \cdot (\mathbf{C}\mathbf{f}_0)$ and $\mathbf{s}_0 \cdot (\mathbf{C}\mathbf{s}_0)$ respectively. Finally, the orthotropic response is reflected in the term $I_{8fs} = \mathbf{f}_0 \cdot (\mathbf{C}\mathbf{s}_0)$. \mathbf{f}_0 and \mathbf{s}_0 are the fiber direction and sheet direction respectively. The volumetric response is composed of the bulk modulus, D , and the Jacobian (determinant) of the deformation gradient, J .

In the LHHM, material constants used to describe the MV and TV have been adjusted to represent the stresses described in (May-Newman and Yin, 1995). Chordae and PM

locations have also been adjusted to simulate complete closure in the neutral RV geometry. Local fiber orientations of the valve and biaxial data describing the isotropic Marlow hyperelastic material response of the chordae were adapted from (Kunzelman and Cochran, 1990).

To capture the Frank-Starling effect, an active material response that mimics time-varying myofiber tension (σ) post electrical activation is given by (Walker et al., 2005):

$$\sigma(t, E_{ff})_{active\ fiber} = T_{max} \frac{Ca_0^2}{2(Ca_0^2 + ECa_{50}^2)} (1 - \cos(\omega)), \quad \text{Equation 18a}$$

$$ECa_{50} = \frac{Ca_{0\ max}}{\sqrt{e^{B(l-l_0)} - 1}}, \quad \text{Equation 18b}$$

$$\omega = \begin{cases} \pi \frac{t}{t_0}, & \text{when } 0 \leq t \leq t_0, \\ \pi \frac{t-t_0+t_r}{t_r}, & \text{when } t_0 \leq t \leq t_0 + t_r, \\ 0, & \text{when } t_0 + t_r \leq t, \end{cases} \quad \text{Equation 18c}$$

$$t_r = ml + b, \quad \text{Equation 18d}$$

$$l = l_r \sqrt{2E_{ff} + 1}, \quad \text{Equation 18e}$$

In Equation 18, T_{max} indicates the maximum active stress that can be achieved in a myofiber; Ca_0 and $Ca_{0\ max}$ represent initial and peak Calcium concentrations in the myofiber; l_0 is the minimum sarcomere length at which active stress develops; l_r is the reference fiber length; t_0 is the time until maximum stress is reached; B , m and b are phenomenological constants; and E_{ff} is the Green-Lagrange strain component in the fiber direction. Figure 9 illustrates corresponding active tension responses at values used in (Walker et al., 2005) and for E_{ff} ranging from 0 to 0.05 (full physiological range).

The stress in the fiber direction will therefore be

$$\sigma_{fiber} = \sigma_{passive\ fiber} + \sigma_{active\ fiber}, \quad \text{Equation 19}$$

And stress in the sheet direction will be

$$\sigma_{sheet} = \sigma_{passive\ sheet} + n * \sigma_{active\ fiber}, \quad \text{Equation 20}$$

Where n is a constant less than one that influences the Ejection Fraction (EF) and Apical Twist (AT). Isotropic time dependent linear viscoelasticity is defined as part of the material constitutive behavior to damp out the high frequency response during ventricular systole (contraction). While cardiac tissue is generally known to exhibit viscoelastic behavior, suitable experimental data on cardiac viscoelasticity were not available; hence, the model incorporates a small amount of viscoelasticity to only eliminate unrealistic transient behavior.



Figure 9 Time-Dependent Active stress. Shaded lines imply a longer relaxation time associated with increased Fiber strain. Arrow represents active stress curve at minimum strain

3. Methodology

In this study, an attempt is made to accurately characterize the complex nonlinear mechanical behavior of the RV during progressive remodeling for both small and large strain parameters. Given the nature of PH, any thorough study of the disease requires modeling of the whole heart to investigate the main etiologies of the disease. Highlighting the interplay between RV dynamics and the TV will greatly add to our understanding of the etiology and intervention policies pertaining to FTR, especially when FTR is a product of RV failure or remodeling. To the best of our knowledge, there are no current studies that can quantitatively evaluate the mechanical parameters leading to RV failure in pulmonary hypertension, nor are there any models of the full heart used to investigate the issue of FTR (Lee et al., 2019; Morgan et al., 2020). We use the LHHM and its simulation framework through myocardial volume reverse remodeling as well as epicardial and endocardial surfaces shrinkage in order to address the clinical observations related to the short and long-term RV reverse remodeling. To that end, we present herein the case of a 72-year-old female symptomatic with chest pain and exertional dyspnea, suffering severe MVR, PH and Left Atrial (LA) dilation, and who has undergone MV replacement. We present a simulation of the full patient heart before and after surgery using the FE method. We also simulate the presence of a TV annuloplasty ring to demonstrate that if annuloplasty is not undertaken it is predicted that the patient post MV-replacement surgery will nonetheless likely develop FTR and RV failure due to excessive cyclical forces on the annulus that lead to Tricuspid Annulus (TA) dilation.

3.1 Reverse Remodeling

3.1.1 Patient Specific Data Acquisition

Patient-specific geometry and cardiac function were obtained from a transthoracic echocardiogram (TTE) and cardiac magnetic resonance (CMR) of the patient who exhibited chest pain and exertional dyspnea, diagnosed with severe mitral regurgitation (MR) and moderate-severe tricuspid regurgitation (TR). The patient underwent bioprosthetic mitral valve replacement (Biologic Epic #29) (Abbott Laboratories, Chicago, IL) and tricuspid valve repair (Ring #30) at the Shaheed Rajaei's Cardiovascular Medical and Research Center in Tehran, Iran. CMR imaging was acquired using a multi-planar MR sequences using truFISP,

truFISP cine, whole heart coronary imaging, 3D contrast-enhanced high-resolution MR angiography of the vessels of the chest and upper abdomen with administration of 20 ml of Gadolinium contrast agent. In order to obtain accurate measurement of peak PAP to model right ventricular geometry, tricuspid valve function, and wall stress in the three-dimension modeling to assess pulmonary arterial hypertension, right heart catheterization was performed.

Pre-operatively, echocardiography and MRI showed bi-atrial enlargement, LA and RA area measured at 36.5 cm² and 27.2 cm², respectively, as measured on CMR. LA volume index estimated at 91 ml/m² (increased from a normal 34 ml/m²), whereas RA index measured at 53 ml/m² (from a normal 21 ml/m²). CMR and TTE showed mild systolic function, with a left ventricular ejection fraction (LVEF) at 47 %; however, LV and RV size were within normal range. LV end-diastolic volume index (EDVI) was measured at 75 ml/m², whereas the right ventricle was measured at 74 ml/m². Velocity flow assessment showed severe mitral regurgitation, thickened leaflets, mild mitral stenosis (mitral valve area = 1.8 cm², mean gradient 5 mmHg), and an associated moderate-severe tricuspid regurgitation as per the TTE, later confirmed by CMR. PAP on echocardiography was found to be 70 mmHg. CMR revealed basolateral LV wall motion abnormality. The radiological demonstration of typical mid-myocardial fibrosis in the basal and mid-septal segments with a linear appearance as well as subepicardial enhancement of the lateral wall, correlating with a non-ischemic dilated cardiomyopathy.

Following mitral valve replacement and tricuspid valve repair, a CMR was repeated. There was a decrease in end-diastolic volume index for the LV and RV, 44.2 ml/m² and 45.5 ml/m², respectively. LVEF mildly decreased post-operatively to 42%. There was an estimated 15% reduction in LA area to 31 cm², resulting in a 30% reduction in LA cavity volume. RA remained normal in size, with an area of 20 cm². Velocity flow mappings showed no mitral regurgitation, with a mild tricuspid regurgitation. There was a significant reduction in pulmonary hypertension to 30 mmHg on repeat TTE. There was persistent global LV and RV hypokinesia, which is compatible with chronic cardiac remodeling as seen with non-ischemic dilated cardiomyopathy.

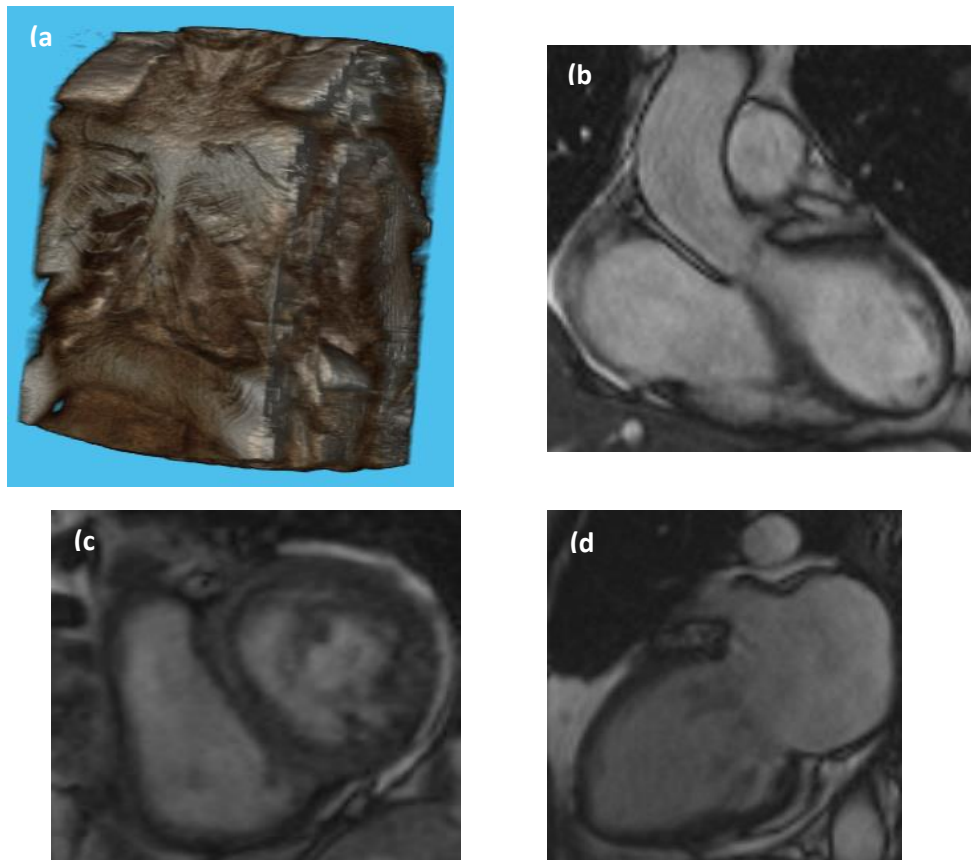


Figure 10 MRI obtained images of patient heart Pre-surgery (a) Shows a 3D volume of the patient chest generated in MATLAB (b) A four-chamber view showing an enlarged RA (c) Short-axis biventricular view with a flattened septum and characteristic D-shaped LV (d) Left-heart view of the LA and LV

Table 3 MRI report of patient End Diastolic Volume, Stroke Volume and Ejection Fraction compared to values in healthy female patients of mean age 43 reported in (Lin et al. 2008)

Cardiac Output	Pre-Surgery	Post-Surgery	Normal (Lin et al., 2008)
LA EDV (ml)	176	123.2	102
RA EDV (ml)	130	91	111.9
LV EDV (ml)	144	85.7	144
RV EDV (ml)	143	88.6	83
LV SV (ml)	68	36	90.7
RV SV (ml)	67	39	48.1
LVEF (%)	47	42	63
RVEF (%)	46.6	44	58

3.1.2 Parametric Study: LA Dilation

According to the chamber volumes corresponding to our patient, the LA was severely dilated pre-surgery, while RA and RV were mildly dilated. In order to implement these morphological changes on LHHM geometry, we adopt a dilation model initially developed by Athanasios et al. (Athanasios, 2018). This methodology uses thermal expansion where thermal strain is computed by the following equation (Abaqus 6.14 User Manual: Thermal Expansion):

$$\boldsymbol{\varepsilon}^{thermal} = (\theta - \theta_0)\boldsymbol{\alpha}(\theta) - (\theta_I - \theta_0)\boldsymbol{\alpha}(\theta_I), \quad \text{Equation 21}$$

Where $\boldsymbol{\varepsilon}^{thermal}$ is the thermal strain, θ is the temperature, θ_0 is the reference temperature at which no thermal strain occurs and θ_I is the initial temperature at the beginning of thermal expansion. In this methodology, an orthotropic coefficient of thermal expansion $\boldsymbol{\alpha}$ was used, with which we defined expansion in fiber and sheet directions. All expanded geometries are extracted from their analyses and used at a zero-stress state in full cardiac beat analyses.

Expansion Pre-surgery: In order to expand the geometry in Abaqus, an initial “preload step” is applied, in which the End Diastolic (ED) Geometry of the heart with fully pressurized chambers is reached. It is then followed by the “Expansion step”, during which we apply a boundary condition to trigger thermal expansion. An expansion coefficient is applied on the corresponding parts (LA, RA, LV or RV). In order to guide expansion in our model, we define expansion coefficients in the Atria in global coordinates, with the direction away from ventricles according to the observed shape of atrial dilation in CMR images. A fiber-dependent expansion applied on the RV is applied, to simulate the effects of the afterload on ventricular fibers. A predefined field (temperature) is applied on that part to trigger dilation. The expansion process is stopped once dilated geometry reaches chamber volumes corresponding to the EDV of the patient, and this heart geometry is then extracted. A brief parametric study investigating of cardiac expansion will be conducted on the RV and RA.

Expansion Post-Surgery: In the case of the heart post MV replacement, the afterload caused by PH was removed, and the ventricular volumes were reduced without hypertrophy or thickening. LA and RA volumes were reduced as well but to a less degree, and it is for this reason, the dimensions of the entire heart were reduced isometrically, and thermal

expansion was applied only on the LA and RA similar to the protocol pre-surgery such that all chambers reach the volumes corresponding to those obtained from echocardiography.

Post remodeling, fiber orientations are readjusted by the algorithm: $\mathbf{e}^{\text{dilated}} = \mathbf{F}\mathbf{e}$, where \mathbf{e} corresponds to those fiber orientations, $\mathbf{f}_0, \mathbf{s}_0, \mathbf{n}_0$, on the reference geometry, \mathbf{F} corresponds to the deformation gradient, and $\mathbf{e}^{\text{dilated}}$ corresponds to them in the dilated geometry. The network of Purkinje fibers in the LHHM is composed of 3D truss elements spanning the endocardium. In order to morph these fibers according to different ventricular geometries, zero-distance mapping constraint described in Equation 22 was enforced between Purkinje nodes and ventricular nodes.

$$P(x, y, z) - N(x, y, z) = P'(x, y, z) - N'(x, y, z), \quad \text{Equation 22}$$

Where $P(x,y,z)$ and $P'(x,y,z)$ correspond to the initial Purkinje fiber nodal coordinates and morphed coordinates respectively, and $N(x,y,z)$ and $N'(x,y,z)$ correspond to the nearest initial ventricular nodal coordinates and morphed nodal coordinates respectively. A schematic of the adjustment methodology employed is illustrated in figure 11 (Fig. 11).

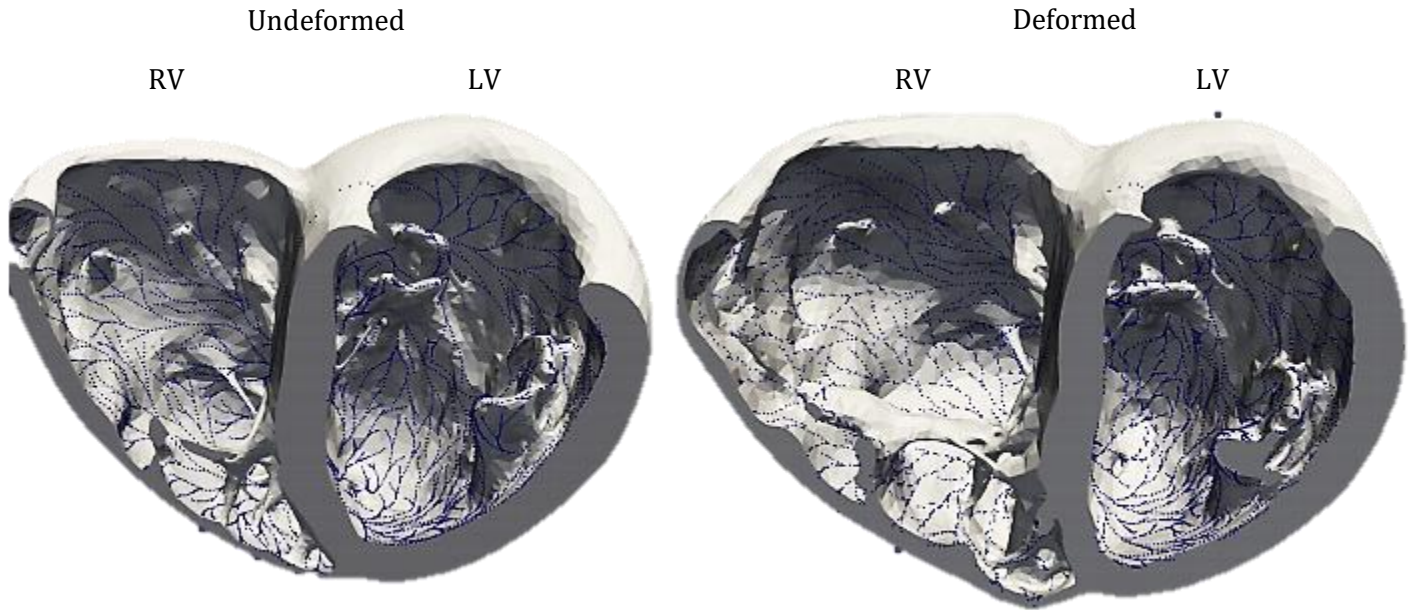


Figure 11 Illustration of Purkinje fibers (blue) reconstruction overlaid on-top of the two-chamber slice of the ventricles (grey). When ventricles are morphed, zero distance is kept between ventricular geometry and Purkinje fiber geometry

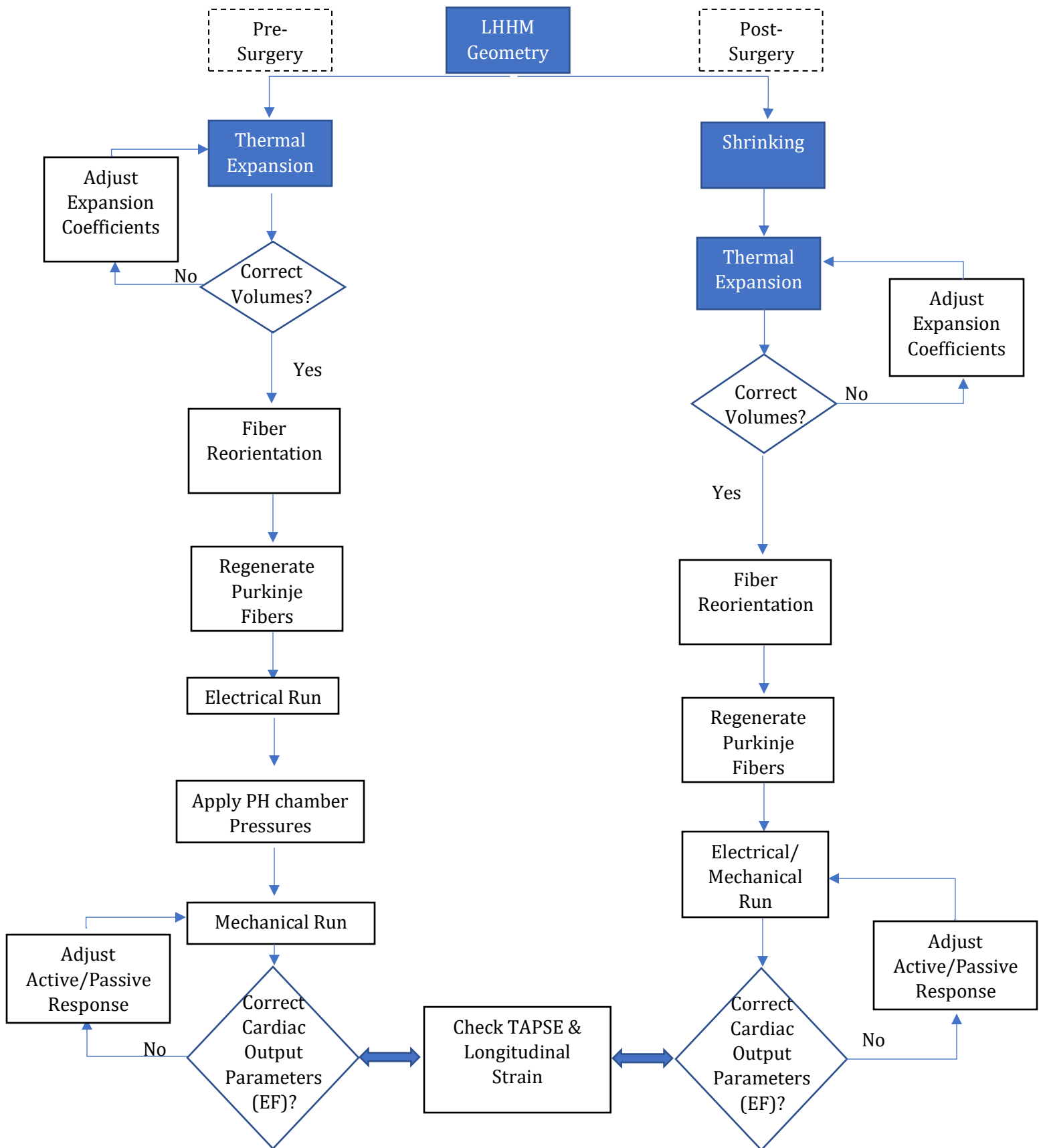


Figure 12 Flow-Chart of Expansion Method applied to simulate Dilatation

3.1.3 Adjustment of Material Properties

Fine tuning of material parameters (Walker et al., 2005) was necessary to obtain the appropriate patient-specific Ejection Fraction. We reflect the opinion of literature on certain parameters, such as increasing stiffness post-surgery as per the authors of (Fujimoto et al., 2012). A breakdown of the expansion method and modification of constants can be seen in figure 12 (Fig. 12). A list of all model parameters will be defined in the Appendix. To investigate the efficacy of our approach to demonstrate RV failure, we will examine the presence of certain disease biomarkers in our model such as TAPSE and GLS, shown in figure 13 (Fig. 13). TAPSE will be measured by the “M-Mode” which is the distance between the basolateral end of the RV and the apex. The length of this distance changes throughout the cardiac cycle, and difference between the diastolic (maximum) distance and the systolic (minimum) distance is TAPSE and indicates the state of the RV (Fig. 13 a,b) (Samad, Alam and Jensen-Urstad, 2002; Bashline and Simon, 2019). GLS will be the average of six element strains on the RV free wall as reported in literature (Lisi et al., 2015). We will also comment on tissue stresses present in our model and compare cardiac output between pre-surgery, and post-surgery geometries.

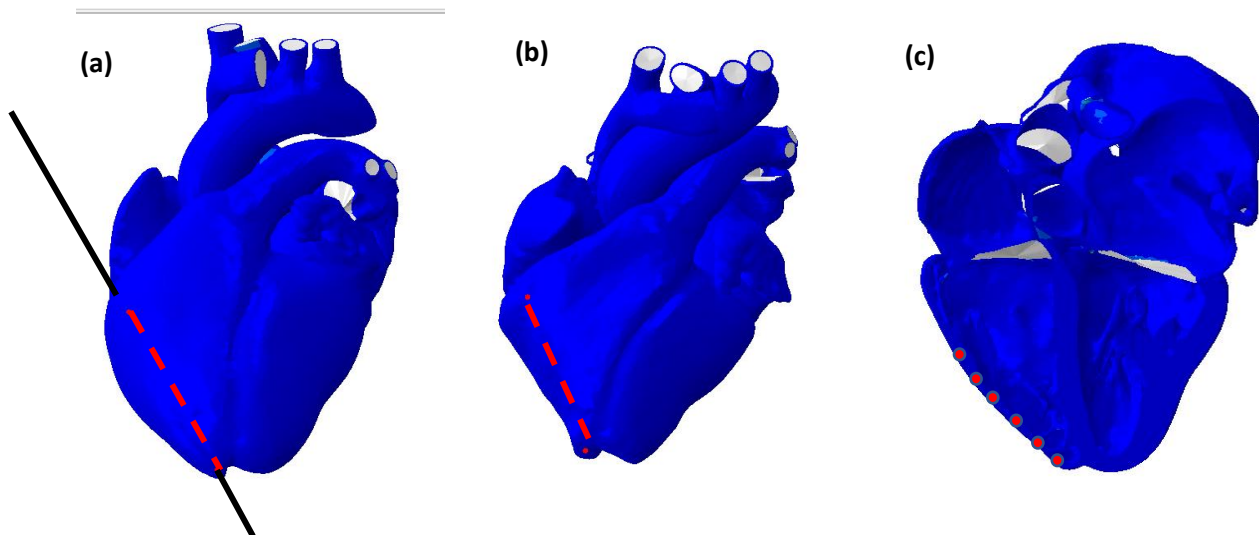


Figure 13 TAPSE is measured as the difference between maximum and minimum lengths in the M-mode (shown in red) (a,b) through the cardiac cycle. Six segments of the RV Free wall have been used to extract circumferential and longitudinal strain (c)

3.2 TV Investigation

3.2.1 TA Forces

The TV and MV were discretized into denser meshes of 21,252 and 70,210 deformable 3D linear tetrahedral elements respectively. Chordae were modeled as truss elements and chordae-TV interactions and TV-RV interactions were defined by distributed coupling, and the chordae were fixed to the Papillary Muscles (PM) using a tie-constraint. The material constants used in this work to describe the MV and TV have been also adjusted to represent the stresses described in May-Newmann et al. (May-Newman and Yin, 1995). Chordae and PM location have been adjusted to simulate complete closure in the neutral RV geometry. The TA in our model is defined as the region of the ventricles to which the valves are attached. Local fiber orientations of the valve and corresponding biaxial data describing the isotropic Marlow hyperelastic material response of the chordae were adapted from Kunzleman et al. (Kunzelman and Cochran, 1990). A 0D-Windkessel model was used to extract fluid pressure across the different cardiac chambers, and patient-specific transvalvular pressure was thus applied to the ventricular sides of the TV leaflets.

To model the post-operative geometry for the patient, their MV geometry must be forgone (due to the replacement). We instead model the effect of the replacement valve and ring using connector elements. This is done by constraining 20 nodes which substitute for suture points between the new ring/valve complex and the ventricles (Baillargeon et al. 2015). Each node is connected to its neighbor by a rigid link in a circumferential formation (Fig. 14 a), to remove relative motion between suture points, and to mimic the mechanical effect of the new ring/MV complex.

Surgical intervention planning for TV repair requires a thorough understanding of the state of the TA. In order to study the behavior of the TA pre- and post-operatively, we further define a hypothetical ring as above for the TA, so that forces measured along the ring would directly reflect TA dynamics in the cardiac cycle. We assign wire connector elements that link 40 ventricular nodes along the TA, using rigid links to constrain their relative motion and to simulate the effect of a rigid annuloplasty ring. Average link length

was 3.74 ± 1.22 mm in the pre-operative geometry and 4.07 ± 2.44 mm in the post-operative geometry.

We also explore the effect of using rigid and semi-rigid links on the forces in the TA for the post-operative geometry. In the semi-rigid case, axial connectors are prescribed an elasticity and a damping, as characteristic of the behavior of a spring-dashpot (Fig. 14 b). The spring element has a stiffness of 8.66 N/mm compared to 10.12 N/mm experimentally determined from a mitral annuloplasty ring (Pierce et al., 2016). Resulting forces on these elements are compared to help elucidate the difference between forces on the TA before MV replacement and after.

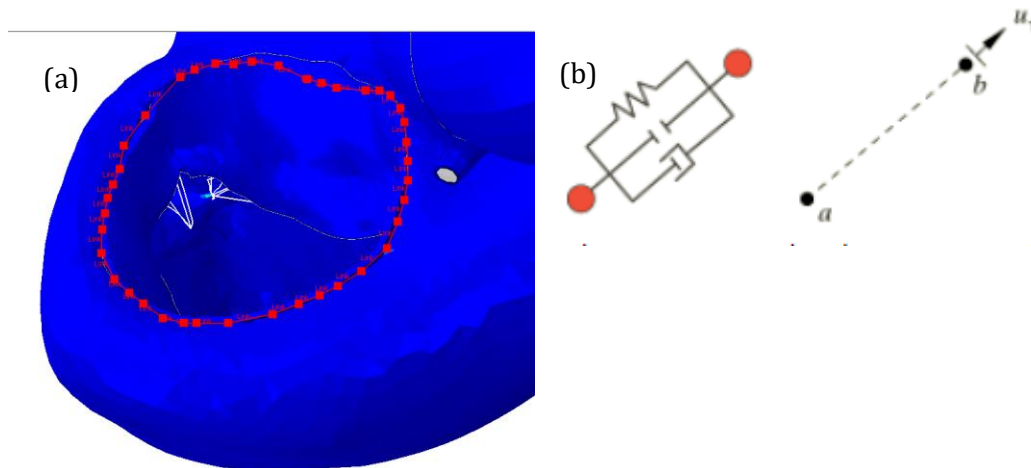


Figure 14 Rigid Links shown in red (a), along with link formulation (b). Links maintain kinematic motion between points a and b (in this case our suture points)

4. Results & Discussion

The dilation method was used to create patient-specific geometry before and after MV surgery. Because it is important to reach all chamber volumes and geometries simultaneously, a study of the parameters inducing dilation was necessary. We observed that dilation of individual chambers did not affect the geometries of neighboring chambers drastically, and so assigning unique dilation properties to each chamber is possible. Since expansion occurs post preload, dilated chambers are pressurized and we investigate the role of preloading which is defined by PH, as well as that of the boundary condition, applied on the RA chamber. An expansion coefficient $\alpha = [0.005, 0.005, 0]$ applied on the RA geometry and 11 thermal expansion trials were applied. Fig. 15 shows the results of the expansions. The behavior shown in Fig.15 shows a tapered reduction with (p) and highlights the non-linearity of the expansion process. A relationship between RA Volume (V) temperature applied (θ), and preload pressure (p) have been fitted using the Non-Linear Least Squares method and R^2 for $V(p, \theta)$ was 0.87, while R^2 of the relationship $V(p, \theta, p\theta, \theta^2)$ was 0.98, indicating a stronger correlation between the RA volume and θ^2 . Four additional expansions were done to test our model, and it showed limitation predicting chamber volume at low preload values, overestimating volumes by 24.74 % and 23.15 %, while accurately predicting volumes with higher p, θ combinations of 0.4511 % and 1.053 %.

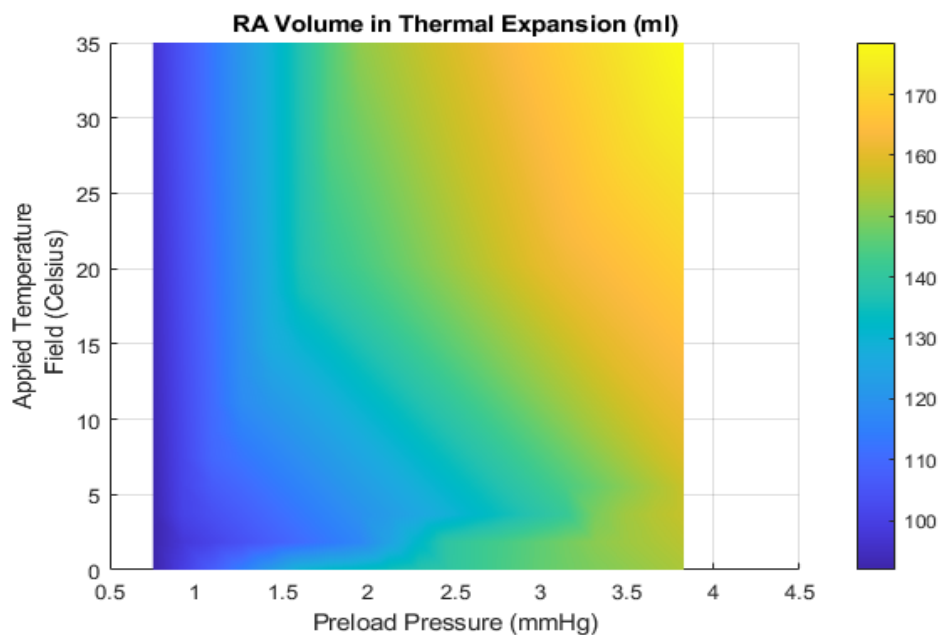


Figure 15 Contour plot interpolating the relationship between RA volume, Temperature applied for thermal expansion, and Preload Pressure. Our model correctly predicts values where preload pressure is high, regardless of applied temperature

A study of the shape of the chambers in PH was made to verify our approach. Although literature generally lacks characterizing the complex shape of Atria, more focus has been given to the ventricles. An analysis of ventricular shape changes by Mauger et al. and Mertens et al. concluded the primary shape change due to pressure overload is the change in volume. Additionally, key shape parameters such as sphericity, which they define as the change in apex-to-base length divided by the chamber width, was also found to have strong correlation with PH incidence (Mertens and Hunter, 2012; Mauger et al., 2019). In addition to these findings, Leary et al. have given focus to the bulging of the RV apex, as well as the reduced global RV strain characterized by TAPSE (Leary et al., 2012). For these reasons, we give attention to these findings in assessing the effectiveness of our approach. The dimensions are shown superimposed on the image of our expanded model (left) and the MRI (right) in figure 16 (Fig. 16). LA and RA represent the long axis of the LA and RA respectively, while MID represents the width at the midmyocardium and AB represents the Apex-to-Base distance. APEX measures the width at the RV apex. All measurements on the MRI were done using MILLENSYS DICOM Viewer (MILLENSYS, Cairo, Egypt). While assessing these dimensions, an assumption about depth is made. Despite not having a one-to-one accuracy of these indices, the trends suggest that we have simulated the case of PH and reduction of afterload post-surgery, observing a decreased RV sphericity and Apical Bulge. The increase in AB/(RA or LA) was not significant, and this is most likely due to the longevity needed for atrial remodeling. A full table of dimensions can be seen in Table 4.

Table 4 Comparison of shape indices between MRI images and our model

	Pre-surgery						Post-surgery					
	RV			LV			RV			LV		
	Model	MRI	Diff.	Model	MRI	Diff.	Model	MRI	Diff.	Model	MRI	Diff.
Sphericity (AB/MID)	0.349	0.343	1.75%	0.623	0.648	-3.86 %	0.351	0.347	1.15%	0.631	0.642	-1.71%
AB/(LA or RA)	1.762	1.714	2.86%	1.397	1.356	3.02%	1.784	1.790	-0.335%	1.389	1.401	-0.857%
RV Apical Bulge (AB/Apex)	4.625	4.549	1.67%	-	-	-	4.850	4.749		-	-	-

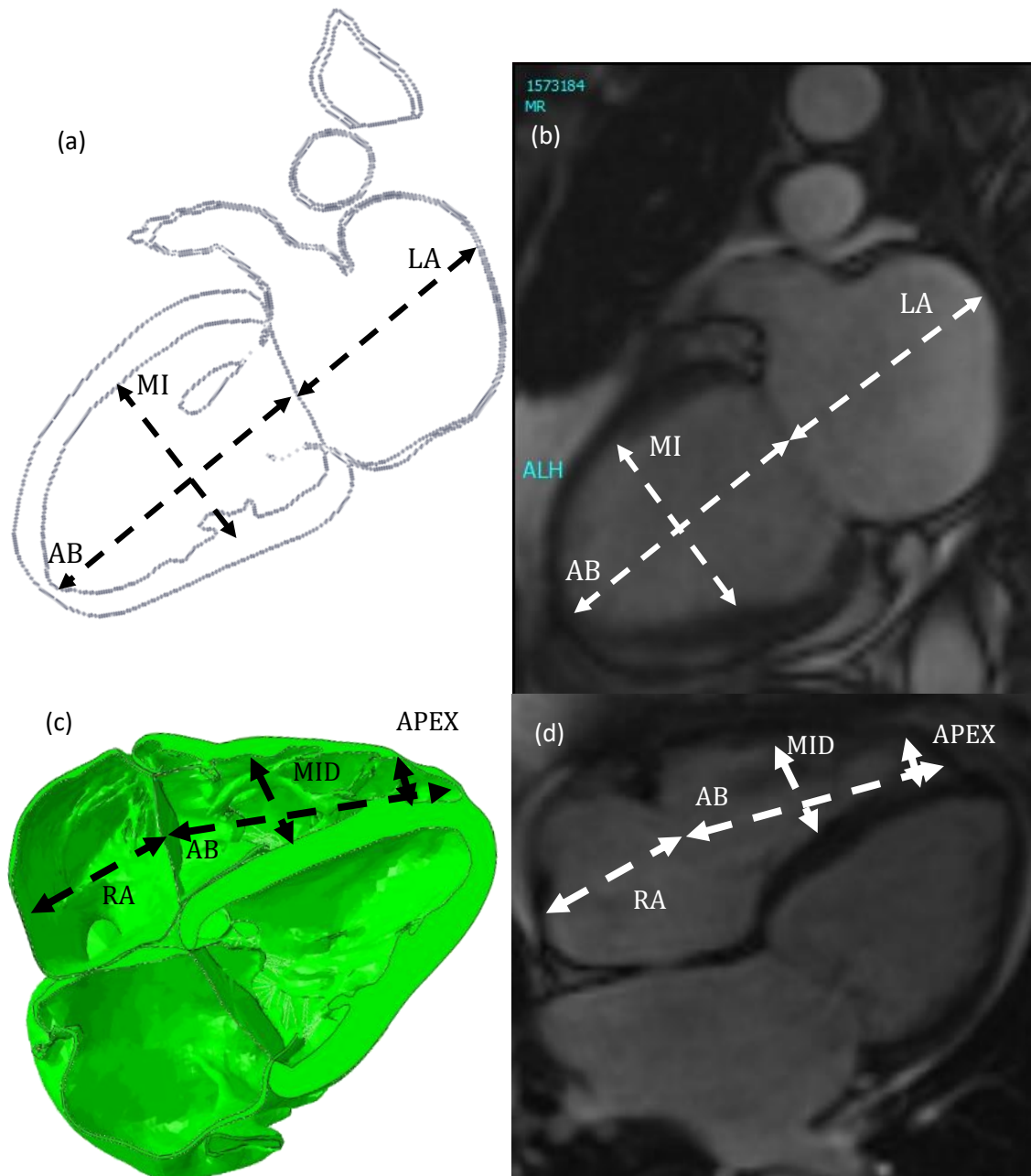


Figure 16 End Diastolic patient geometry pre-surgery in a left side view (a,b) and a 4-chamber view (c,d). A limitation of thoracic-chest CMR imaging lies in the patient stillness during 45 -50-minute sessions. Paraview was used to define the location of the cuts. Since the MRI cuts were midpoints between frames, the 3D model cuts were taken across the center of the heart.

After replication of volume and shape, we note a severe mPAP of 64 mmHg pre-surgery and 38 mmHg post-surgery. Figure 17 (Fig. 17) highlights the increased pulmonary load, and Figure 18 (Fig.18) further stresses the compliant response of the artery pre-surgery, as the ratio between peak systolic PAP and mPAP is lower pre-surgery (1.39) than that post-surgery (2.13).

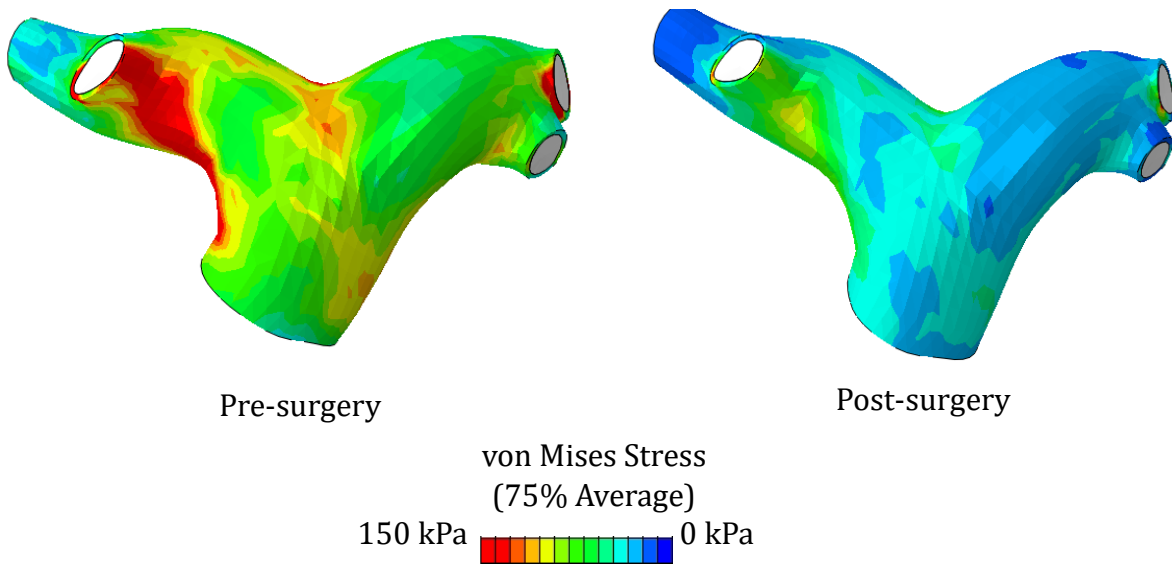


Figure 17 Stress distribution in the End Diastolic pulmonary trunk shows an increase in stress and bulging of the compliant artery in the case of elevated mPAP.

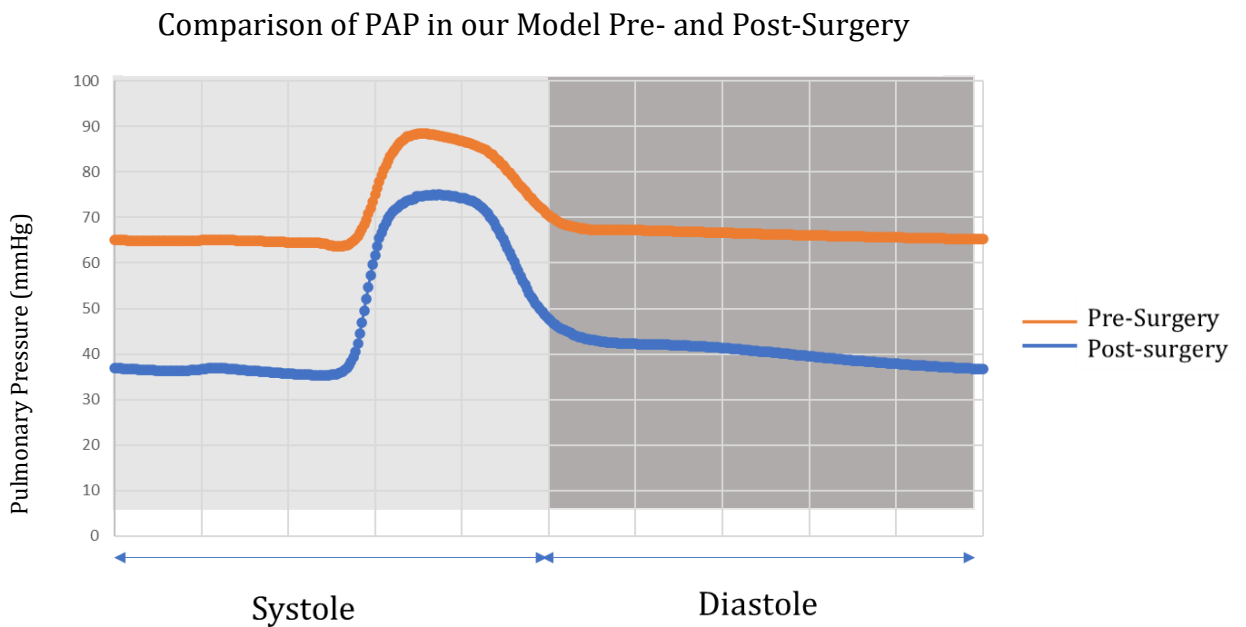


Figure 18 Pulmonary pressure profile shows the difference between pulmonary pressure in our model and the increase in peakPAP/mPAP ratio after surgery due to left-side failure relief

An important aspect of our patient is the left-side failure associated with MR. The systolic function of the simulated heart geometry correctly demonstrated regurgitant MV (Fig. 19), and the ventricles post-surgery continue to exhibit a reduced EF, albeit at a smaller volume. Reduction of cardiac contractility has helped us achieve the correct LVEF which we demonstrate in our model to be 48.77 % compared to the 47 % obtained via echocardiography. Both are lower compared to a healthy 58 %. Similarly, our post-surgery geometry showed a 44.87 % compared to a 42 % in the patient. LA dilation in pre-operation geometry was the main cause of MR in our model, demonstrating accurate portrayal of left-side failure in our model. With these key indices of LV failure presented, we are confident in our model's ability to demonstrate this aspect of the patient. Systolic activity of the LV is

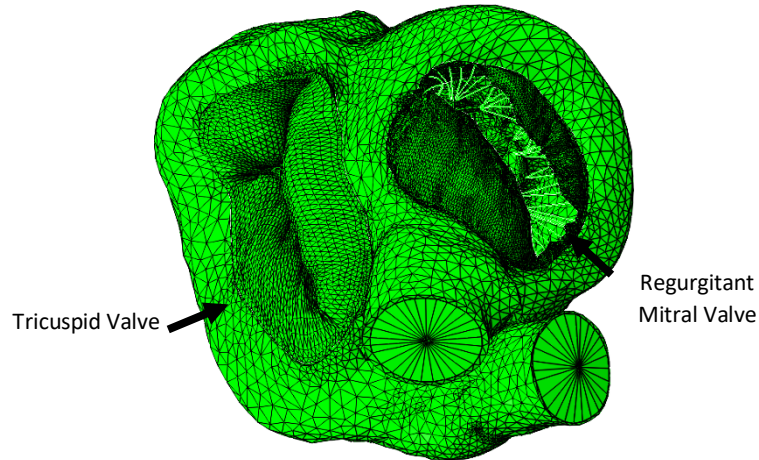


Figure 19 Atrial view of the mid-systolic biventricular pre-operation geometry. Meshing of the ventricles, valves and chordae is shown and incomplete coaptation of the MV can be seen. RA and LA geometries were removed for clarity.

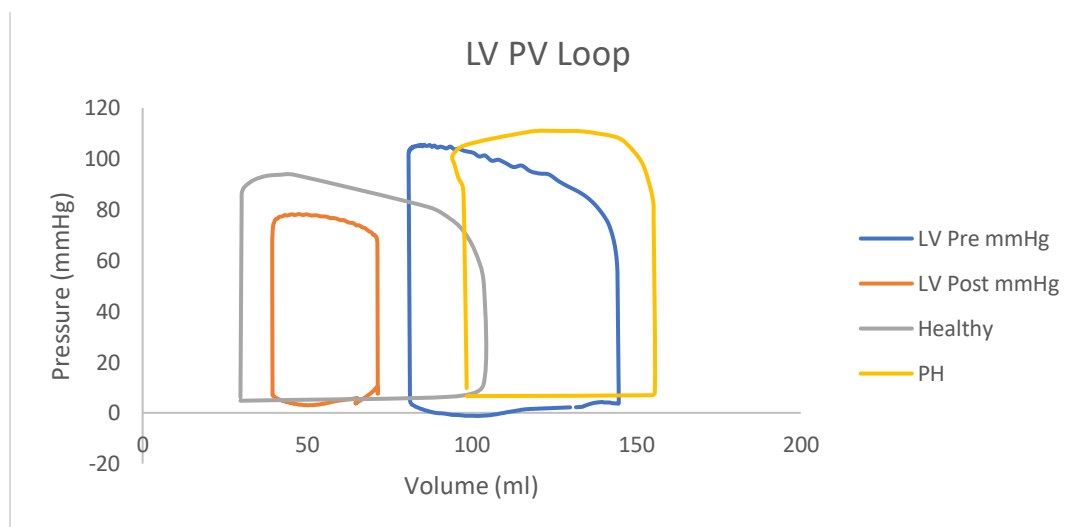


Figure 20 LV cardiac output parameters in our model demonstrated along with data from (Xi et al., 2017). The remarkable reduction in LV volume after removal of the afterload is visible.

shown in Figure 20 (Fig. 20) along with a comparison from literature concerning PH (Xi et al., 2017).

On the addressing of RV failure, we investigate the cardiac output of the RV as well as other markers associated with it. RVEF in our model pre-surgery was 42.81 % compared to 46.6 % in the patient. Post-surgery, we also report 43.54 % in the model compared to a 44 % observed in the patient. In addition, we show a decrease in Global Longitudinal Strain (GLS) characterized by TAPSE. We report a TAPSE of 13.78 mm pre-surgery and 14.48 mm post-surgery, which leads us to conclude that the patient is at risk of RV failure pre-surgery and has mildly reduced in risk post-surgery. It is generally agreed upon that TAPSE < 16-18 mm is characteristic of reduced RV function and imminent RV failure (CMR Guidelines, 2010; Modin et al., 2019). We further studied RV strain and circumferential strain reported in our

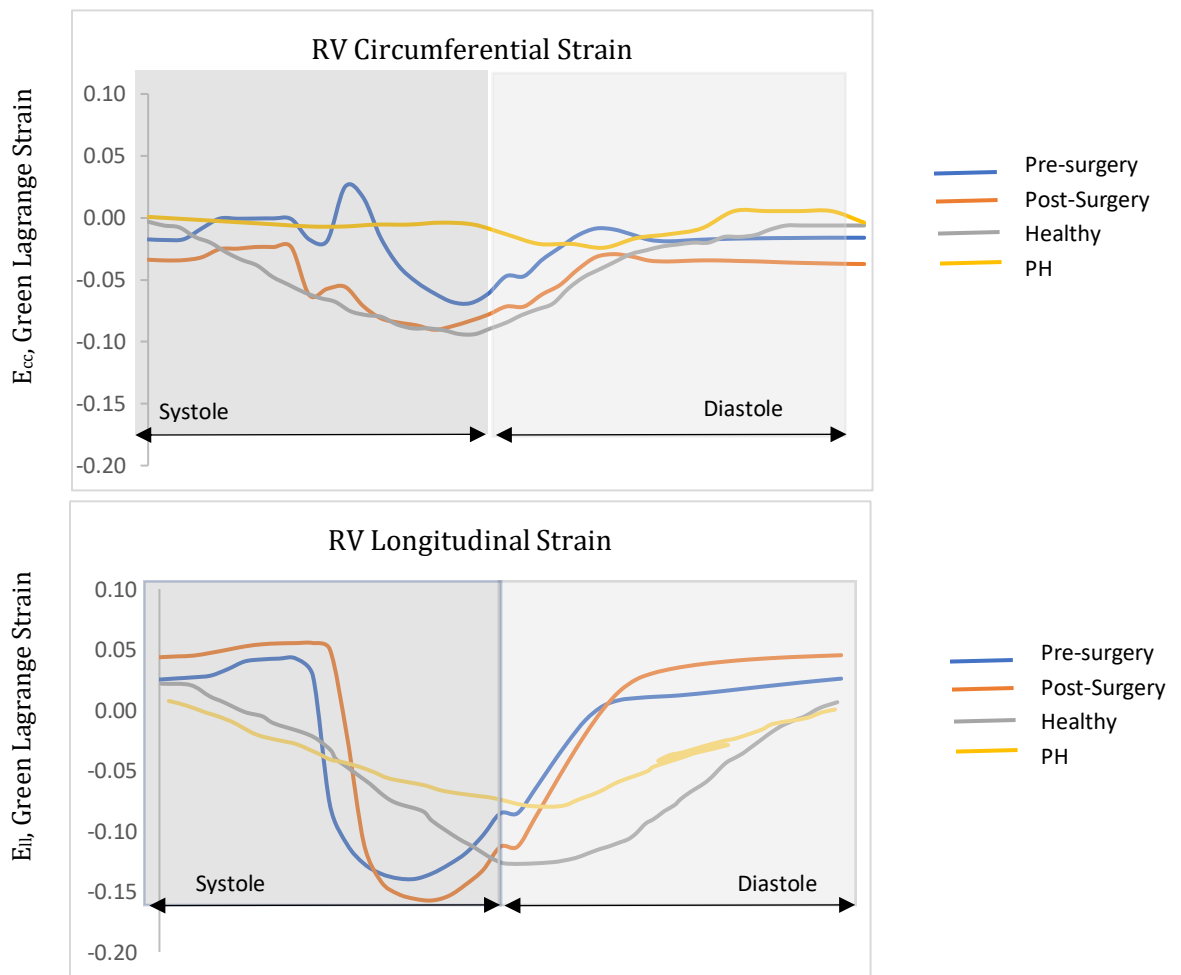


Figure 21 Profile describing Circumferential and longitudinal strain compared to data reported in (Xi et al., 2017) and (Finsberg et al., 2019) respectively.

model (Fig. 21), which shows a movement from diseased values to normal patient values according to reporting (Xi et al, 2017). Furthermore, longitudinal strain also reported in our model leads us to a similar conclusion when compared to literature patients of an average age 52 years (Finsberg et al., 2019).

An added aspect of FE modelling is insight it gives on stress distribution. We levy these insights to report wall stresses in the RV and LV. This is an important step in

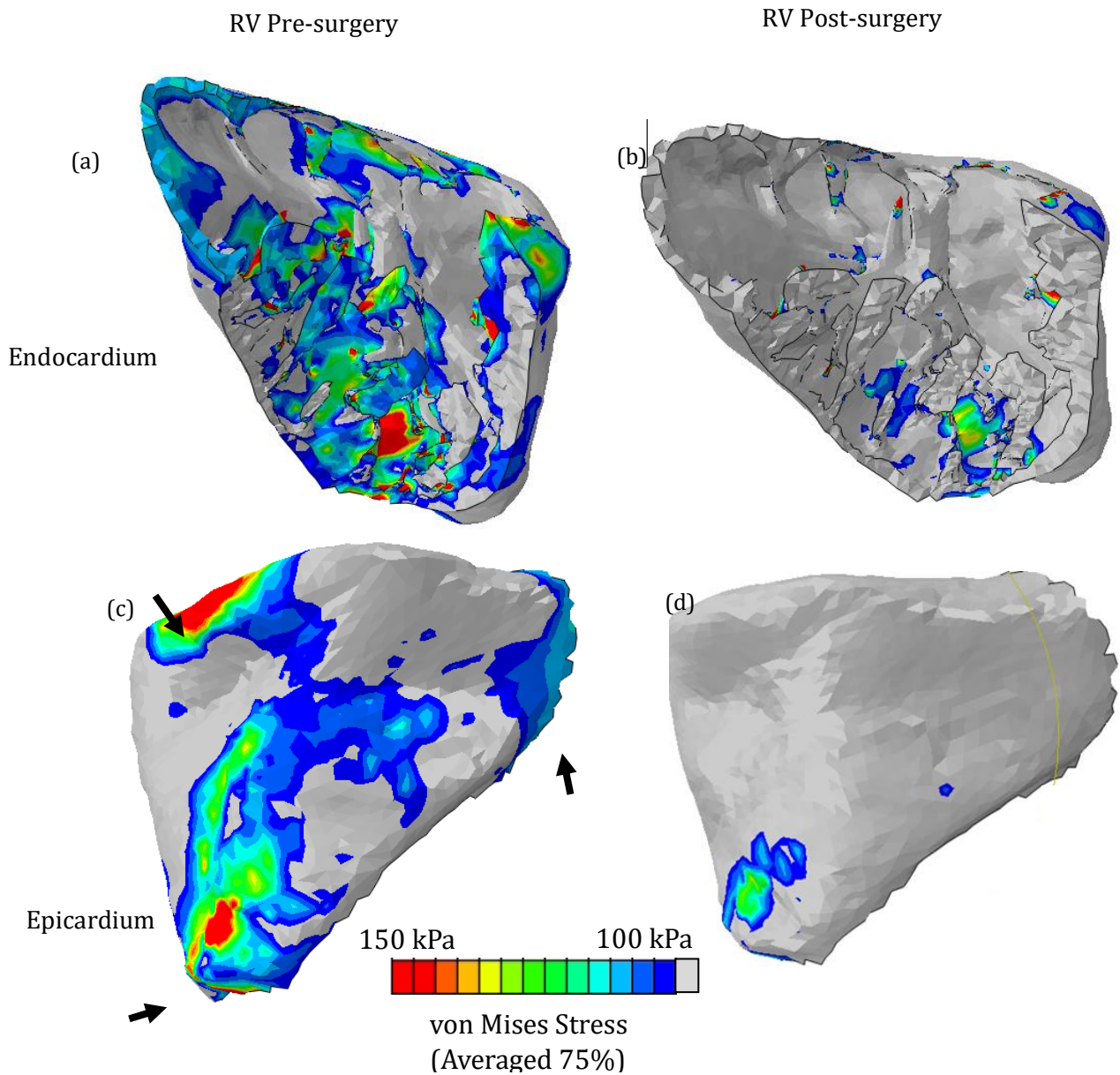


Figure 22 RV mid-systolic stress in the RVFW shows higher stresses in regions corresponding to PH associated shape change in (Leary et al., 2012; Mertens and Hunter, 2012)

investigating the onset of RV dilation and Hypertrophic cardiomyopathy. Our model shows the large average stress on the apical-lateral RV Free Wall (RVFW), the RV outflow tract, and the basal RV near the TA during systole pre-surgery (Fig. 22). This is in accordance to findings of shape changes in PH reported (Leary et al. 2012). Further analysis of transmural

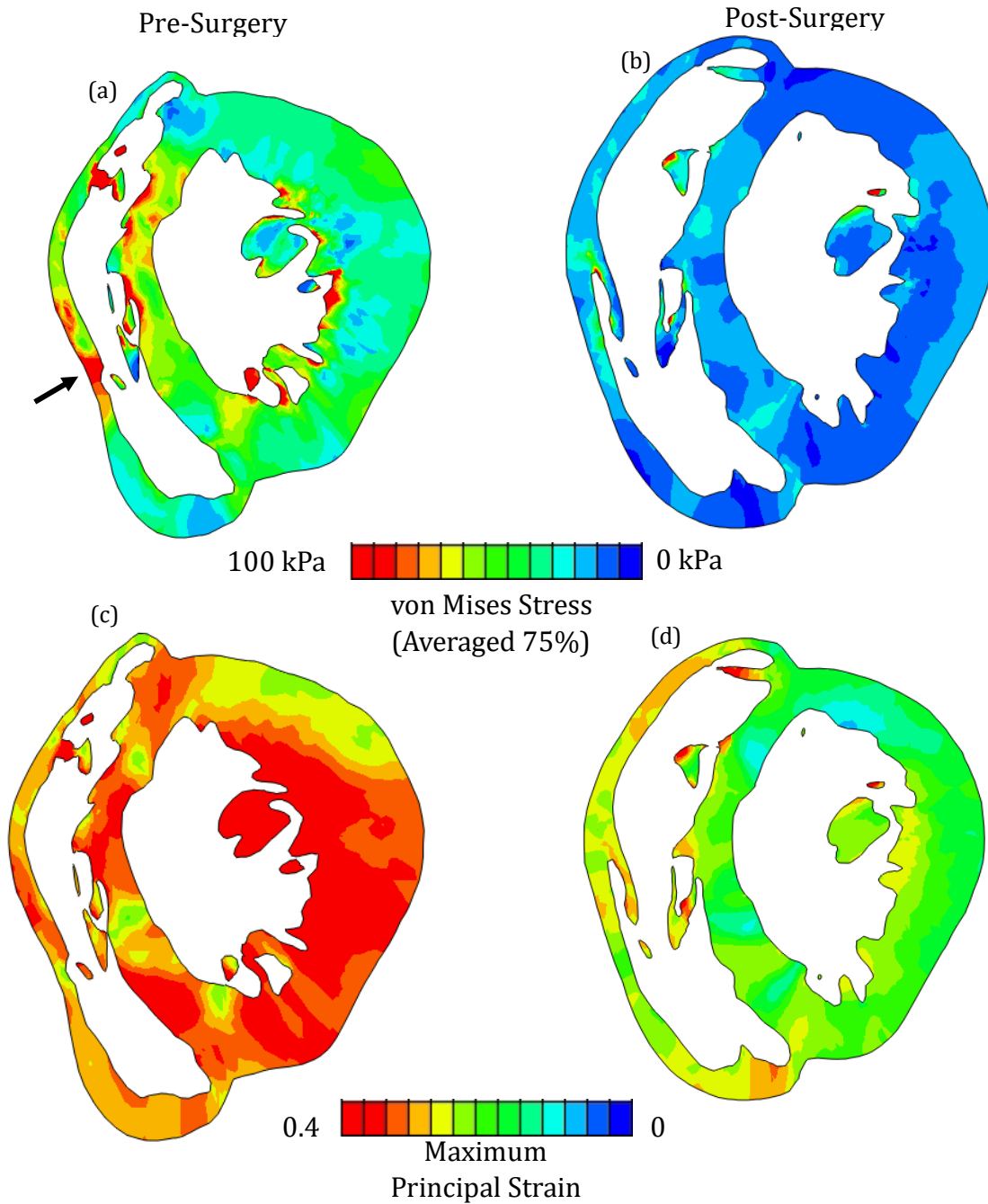


Figure 23 Transmural End-Systolic stress and strain of the ventricles at the mid-myocardium. Stresses are much higher in the Pre-Surgery indicating location of possible dilation in RV (black arrow)

stress shows maximum stresses at the mid-myocardial RV septum which would dilate in adjustment with Laplace's Law (Fig. 23) (Charalampopolous et al., 2018).

Transmural End Diastolic stresses show a marked distribution in LV stress and no significance in change of RV stress (Fig. 24). It is important to note the severe reduction in ventricular size (volume) post-surgery, that occurred due to stiffening developed to

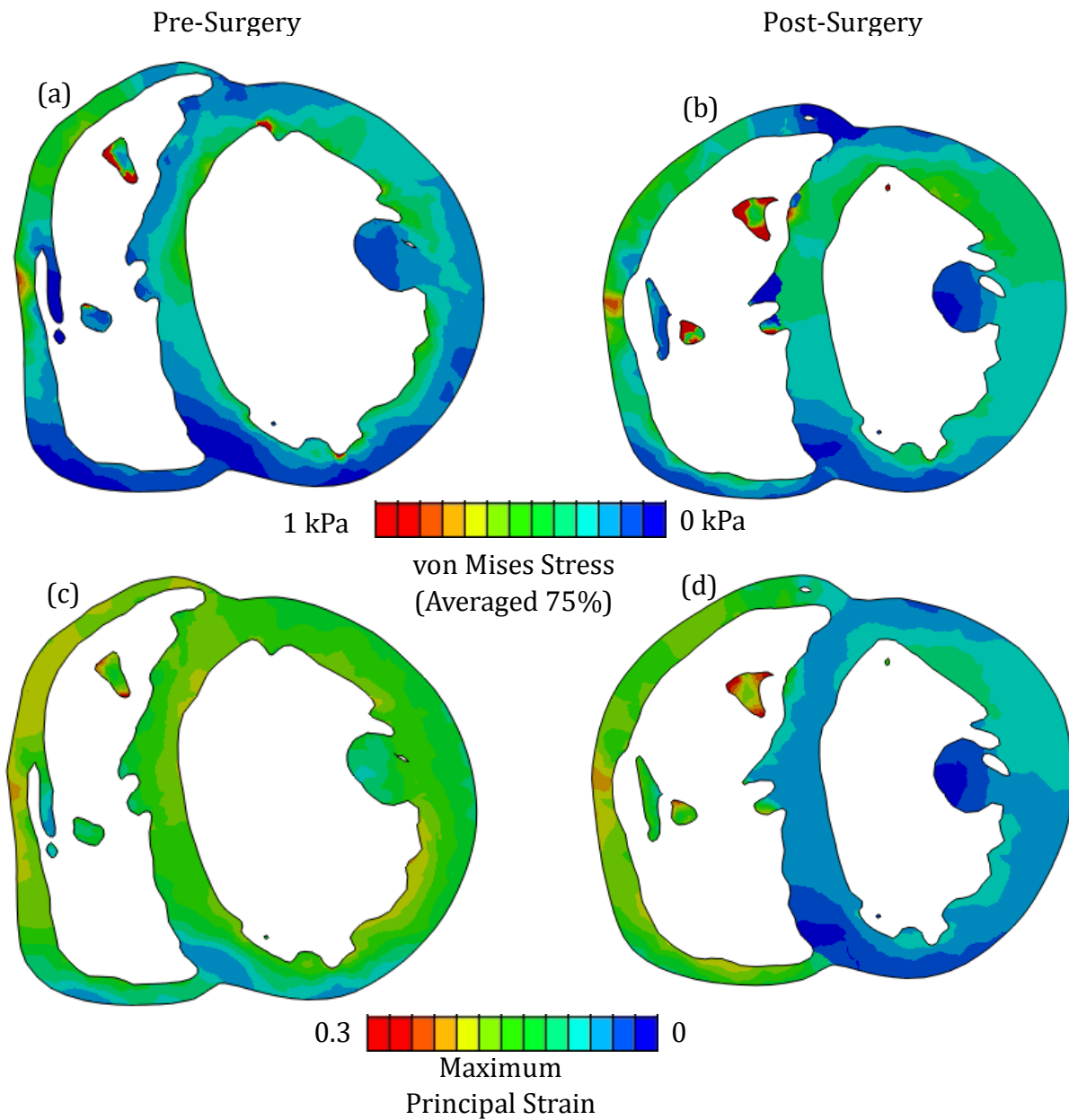


Figure 24 Transmural End Diastolic stress and strain of the ventricles at the mid-myocardium. LV stress is increased after surgery due to the Frank-Starling effect

compensate for an increased afterload (Gaasch and Meyer, 2008). A wide-spread load-sharing is visible in LV stress can be explained according to the Frank-Starling, where the maximum load from blood pressure at the EDV creates lengthening and tension in the LV myofibers with a now-healthy afterload (Huikuri, 1983). The loading across the LV wall is also more distributed indicating a more optimum use of full fiber musculature optimally.

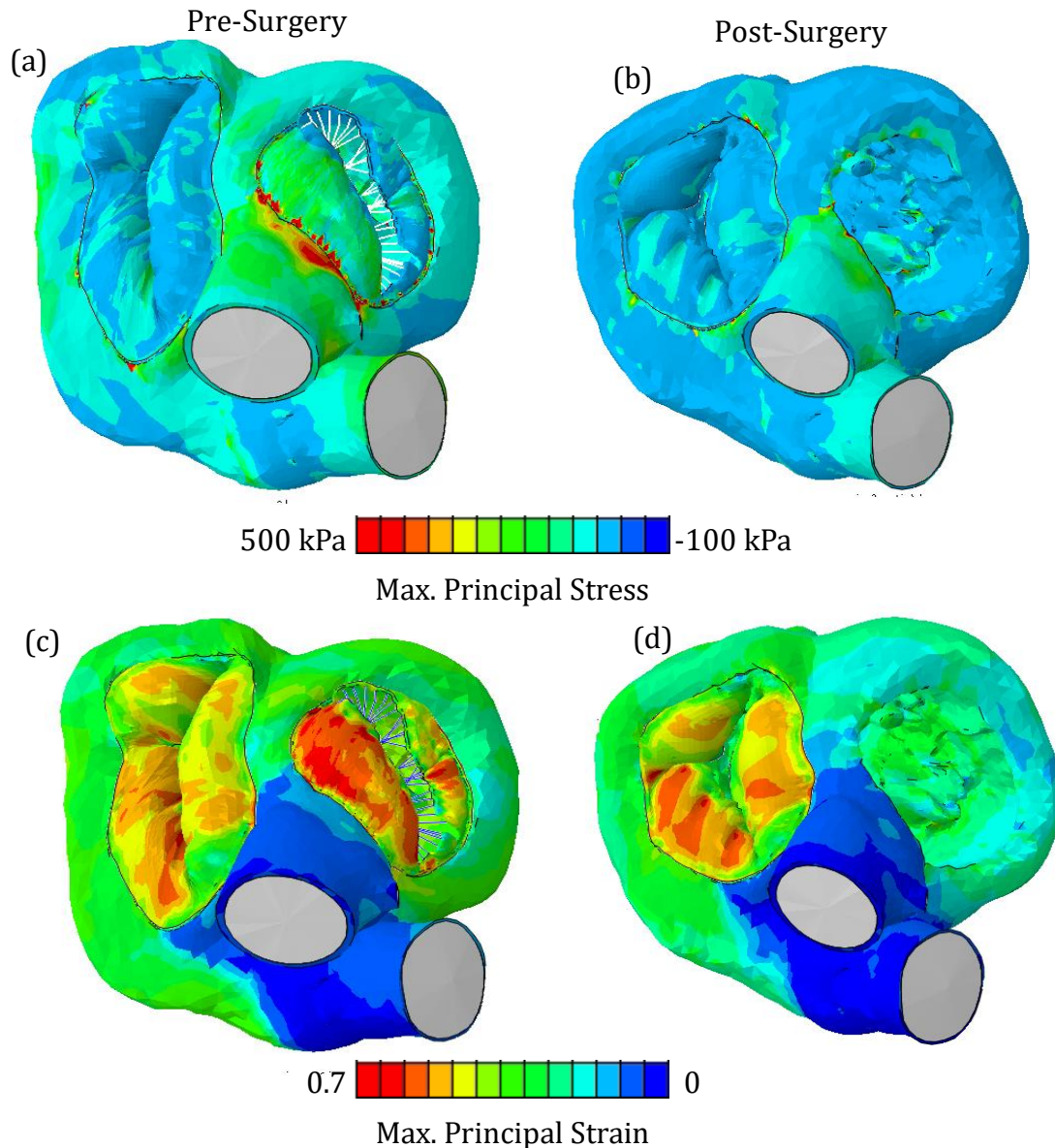


Figure 25 Mid-systolic stress (a,b) and strain (c,d) distribution in TV/MV and ventricles in pre-operation and post-operation. The replacement of the MV with an annuloplasty ring shows a clear reduction in stress and strain at the Mitral Annulus (MA)

ED TA diameter measured from the septal segment to the lateral segment was 46.24 ± 5.26 mm. Maximum principle stress was largest at the MV - aortic root, and maximum principle strain is largest at TV and MV leaflet bellies, with the largest strain in being located in the Anterior Tricuspid Leaflet (ATL) compared to the other TV leaflets (Fig. 25 a,c). Post-operative geometry also showed remodeling of the TA shape to be more rounded, and the ED TA annulus was reduced slightly to 44.06 ± 1.11 mm. The replaced MV has noticeably decreased stress at the aortic root (Fig. 25 b), as well as an increased strain distribution on TV leaflets (Fig. 25 d). We report TV stresses and stress distributions in agreement with Kong

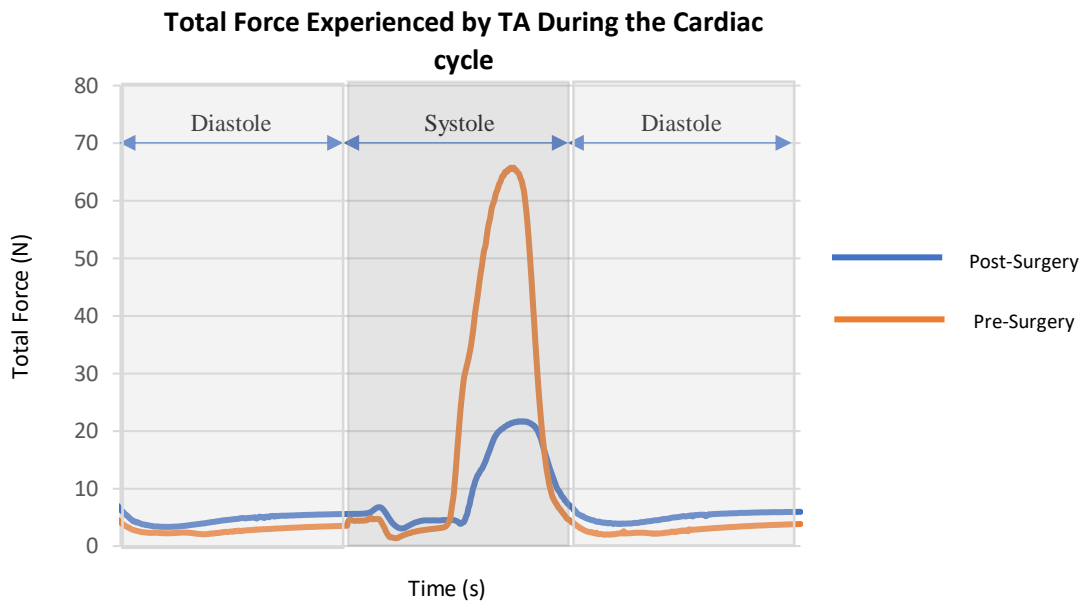


Figure 26 Comparison of forces on the TA shows a higher diastolic force post-operation suggesting TA dilation is more likely. Reduced force during systole also suggests a loss of the role of the TA in coaptation

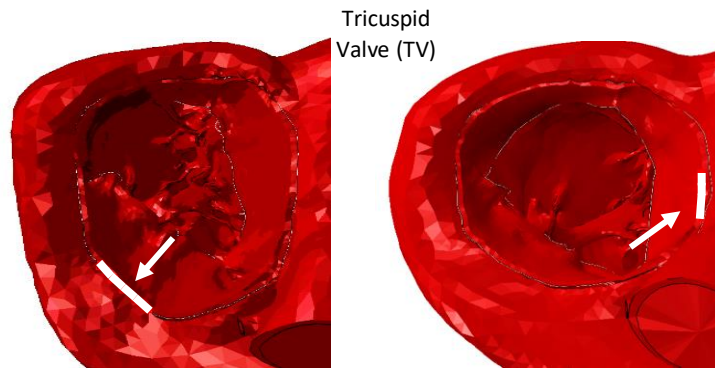


Figure 27 The location of the TA sections exhibiting the largest forces in pre-operation and post-operation geometries. (white)

et al. and Singh-Gryzbon et al. (Kong et al., 2018; Singh-Gryzbon et al., 2019). RA dilation pre-operation, and its size reduction post-operation, created a TV diameter > 40 mm, which indicates the need for TV repair (Dreyfus et al., 2015; Verdonk et al., 2018). A comparison of forces exerted by the TA showed post-operative TA to have a higher force (~2 N) in diastole while pre-operative TA exhibited a remarkably larger force during the systolic phase (~ 42 N) (Fig 26).

The segment of TA undergoing the highest forces in the pre-operative geometry were located at the antero-lateral segment of the TA with a peak average force of 2.990 ± 0.038 N, while post-operative geometry underwent the highest forces at the septal region with a peak average force of 1.144 ± 0.020 N (Fig. 27). Analysis of the forces on TA suggest that during the cardiac cycle, TA widening post operation was larger indicating that over time, TA would dilate outwards. Moreover, TA contraction was shown to be significantly reduced post-operation, indicating valve closure would be impaired with time. This, along with the enlarged TA diameter, and the patient undergoing MV replacement, present the key markers for which the ACA/AHA guidelines recommend TV repair (ACA/AHA 2006 Guidelines, 2006).

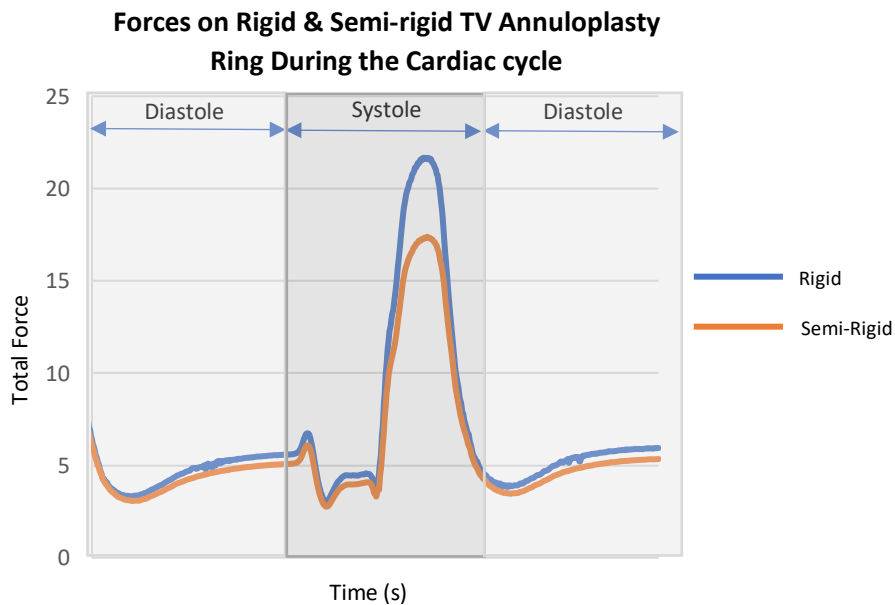


Figure 28 A graph of total forces on rigid and semi-rigid rings shows a reduction of forces during the contraction, reflecting a reduced likelihood of dehiscence – or suture would trauma.

Table 5 Comparison of Forces on constrained Pre-Operative and Post-Operative Geometry

	Constrain Type	Max. (N)	Min. (N)	Average (N)
Pre-Operative	Rigid	65.54	1.38	12.05
Post-Operative	Rigid	21.67	3.06	7.50
	Semi-Rigid	17.39	2.77	6.48

After ascribing an axial behavior to the links on the post-operative geometry, a significant reduction in total force was observed on contraction (Fig. 28). A breakdown of TA forces is shown in Table 5. In the comparison of rigid and semirigid rings, our model demonstrated larger forces on rigid constraints, which suggests a more likely failure mode in accordance with clinical findings (Pfanmüller et al., 2012). A more detailed description of the mechanical properties can be incorporated in the connector elements, which can more accurately represent an annuloplasty ring.

Summary of key findings reported in our model:

- Left-side failure pre-surgery and reduced cardiac output pre-surgery and post-surgery is demonstrated (Gaasch and Meyer, 2008)
- Right-side markers of GLS such as TAPSE and circumferential/longitudinal strain suggest partial recovery of RV failure parameters post-surgery as per (Xi et al., 2017) and (Finsberg et al., 2019)
- RV systolic wall stress decreases post-surgery, indicating reduced propensity for RV dilation or RV failure in agreement with to (Charalampopolous et al., 2018).
- LV volume decreased and stress distribution increased post-surgery as per the findings of (Hikuri, 1983).
- RA/LA dilation caused MR in our model and remodeling of the TA
- Simulating MV replacement showed a decrease MA stresses, and TA remodeling
- Post-operative TA forces were higher than preoperative forces in diastole, but significantly lower in systole
- Semi-rigid links undergo less forces which is safer in cases of possible suture tear (Pfanmüller et al., 2012)

5. Conclusion & Future Works

The Living Heart Project offers researchers a robust computational platform to study the heart in a way that was never possible. The aim of this study was to apply this platform and developed techniques to analyze a patient-specific case-study. The case presented diseased features of the heart pertaining to the geometry and cardiac function, as well as diseased blood flow. This study demonstrated the ability of our FE approach to address a patient-specific problem, and its ability to present medical practitioners with a decision-making tool in the case of FTR and TV repair. We have presented our approach to simulate PH and left-side failure associated with it, as well as subsequent markers for RV failure and the possible need for intervention.

Although governing equations of the LHHM are based on phenomenological parameters and not physiological laws, this platform has shown great potential for applications in cardiology. The long-term changes in tissue composition and cellular structure do not have a current application in the LHHM. A general observation on the LHHM modeling of valve dynamics is the instability associated with large deflections. Regurgitant valves exhibit higher stresses at the annulus, and the meshing at this location often undergoes excessive distortion and the explicit solution at these elements does not converge. Employing an idealized shape of the TV and MV instead of segmentation is a clear limitation of our approach; however, our focus is not to study valve behavior alone, but rather the behavior of the ventricle-valve-chordae complex. Furthermore, the description of the TA in our model is highly simplified, not taking into account the tiered nature of the TA which transitions from a cardiomyocyte-dominant tissue to a cell-free collagenous tissue. The use of 40 nodes, corresponding to 40 suture locations was arbitrary, and this, no doubt, plays a role in the magnitude of forces on the TA.

This study addressed one patient, and in the future, we look forward to tackling a wider array of patients with a longitudinal aspect post-surgery, and integrating additional numerical techniques including FSI to model dilation and valve dynamics. Our approach can also be used to study several scenarios for TV repair using ring annuloplasty, giving insight into forces and stresses that can be invaluable to the understanding of repair and its efficiency. The design of compliant mechanisms, along with development of bio-grade 3D

printing technology offers a promising path to investigate. Furthermore, suture location and suture frequency, as well as ring size all play a role in ring TV repair success and deserves further exploration using our approach.

References

- ACC/AHA 2006 Guidelines for the Management of Patients with Valvular Heart Disease: Executive Summary. *Circulation*, 114(5), pp. 450-527, 2006. Available:10.1161/circulationaha.106.177303.
- Angelini, A., Ho, S., Anderson, R., Davies, M. and Becker, A., 1988. A histological study of the atrioventricular junction in hearts with normal and prolapsed leaflets of the mitral valve. *Heart*, 59(6), pp.712-716.
- Athanasios, A., 2019. A computational model for dilated cardiomyopathy: morphology and electromechanics. M.Sc., Thesis, The American University in Cairo. Digital Archive and Research Repository (DAR).
- Avazmohammadi, R., Mendiola, E., Li, D., Vanderslice, P., Dixon, R. and Sacks, M., 2019. Interactions Between Structural Remodeling and Hypertrophy in the Right Ventricle in Response to Pulmonary Arterial Hypertension. *Journal of Biomechanical Engineering*, 141(9).
- Aversa, A. and Careddu, E., 2017. *Image-Based Analysis of Tricuspid Valve Biomechanics: Towards A Novel Approach Integrating In Vitro 3D-Echocardiography And Finite Element Modelling*. M.Sc. in Biomedical Engineering. Politecnico Milano.
- Badano, L., Muraru, D. and Enriquez-Sarano, M., 2013. Assessment of functional tricuspid regurgitation. *European Heart Journal*, 34(25), pp.1875-1885.
- Baillargeon, B., Costa, I., Leach, J., Lee, L., Genet, M., Toutain, A., Wenk, J., Rausch, M., Rebelo, N., Acevedo-Bolton, G., Kuhl, E., Navia, J. and Guccione, J., 2015. Human Cardiac Function Simulator for the Optimal Design of a Novel Annuloplasty Ring with a Sub-valvular Element for Correction of Ischemic Mitral Regurgitation. *Cardiovascular Engineering and Technology*, 6(2), pp.105-116.
- Barnett, C. and Selby, V., 2015. Overview of WHO Group 2 Pulmonary Hypertension Due to Left Heart Disease. *Advances in Pulmonary Hypertension*, 14(2), pp.70-78.
- Bashline, M. and Simon, M., 2019. Use of Tricuspid Annular Plane Systolic Excursion/Pulmonary Artery Systolic Pressure as a Non-Invasive Method to Assess Right Ventricular-PA Coupling in Patients With Pulmonary Hypertension. *Circulation: Cardiovascular Imaging*, 12(9).
- Belluschi, I., Del Forno, B., Lapenna, E., Nisi, T., Iaci, G., Ferrara, D., Castiglioni, A., Alfieri, O. and De Bonis, M., 2018. Surgical Techniques for Tricuspid Valve Disease. *Frontiers in Cardiovascular Medicine*, 5.

- Bordas, R., Gillow, K., Gavaghan, D., Rodriguez, B. and Kay, D., 2012. A Bidomain Model of the Ventricular Specialized Conduction System of the Heart. *SIAM Journal on Applied Mathematics*, 72(5), pp.1618-1643.
- Bessler, C., Meduri, C. and Lurz, P., 2017. Transcatheter Treatment of Functional Tricuspid Regurgitation Using the Trialign Device. *Interventional Cardiology Review*, 13(01), p.8.
- Buckberg, G., Coghlan, H. and Torrent-Guasp, F., 2001. The Structure and Function of the Helical Heart and Its Buttress Wrapping. VI. Geometric Concepts of Heart Failure and Use for Structural Correction. *Seminars in Thoracic and Cardiovascular Surgery*, 13(4), pp.386-401.
- Carpentier, A., Deloche, A., Dauplain, J., Soyer, R., Blondeau, P., Piwnica, A., Dubost, C. and McGoon, D., 1971. A new reconstructive operation for correction of mitral and tricuspid insufficiency. *The Journal of Thoracic and Cardiovascular Surgery*, 61(1), pp.1-13.
- Charalampopoulos, A., Lewis, R., Hickey, P., Durrington, C., Elliot, C., Condliffe, R., Sabroe, I. and Kiely, D., 2018. Pathophysiology and Diagnosis of Pulmonary Hypertension Due to Left Heart Disease. *Frontiers in Medicine*, 5.
- CME Exam for Guidelines for the Echocardiographic Assessment of the Right Heart in Adults: A Report from the American Society of Echocardiography. *Journal of the American Society of Echocardiography*, 23(7), pp. 786-788, 2010. Available: 10.1016/j.echo.2010.05.022.
- Cohen, S., Sell, J., McIntosh, C. and Clark, R., 1987. Tricuspid regurgitation in patients with acquired, chronic, pure mitral regurgitation. *The Journal of Thoracic and Cardiovascular Surgery*, 94(4), pp.488-497.
- Chin, K. and Coghlan, G., 2012. Characterizing the Right Ventricle: Advancing Our Knowledge. *The American Journal of Cardiology*, 110(6), pp.S3-S8.
- Dabiri, Y., Yao, J., Sack, K., Kassab, G. and Guccione, J., 2019. Tricuspid valve regurgitation decreases after mitralclip implantation: Fluid structure interaction simulation. *Mechanics Research Communications*, 97, pp.96-100.
- David, T., David, C. and Manhiot, C., 2015. When is tricuspid valve annuloplasty necessary during mitral valve surgery?. *The Journal of Thoracic and Cardiovascular Surgery*, 150(5), pp.1043-1044.
- Dreyfus GD, Martin RP, Chan KM, Dulguerov F, Alexandrescu C., 2015. Functional tricuspid regurgitation: A need to revise our understanding. *Journal of the American College of Cardiology*, 65(21), pp.2331-2336.

- Delcroix, M., Vonk Noordegraaf, A., Fadel, E., Lang, I., Simonneau, G. and Naeije, R., 2012. Vascular and right ventricular remodelling in chronic thromboembolic pulmonary hypertension. *European Respiratory Journal*, 41(1), pp.224-232.
- Dwivedi, G., Mahadevan, G., Jimenez, D., Frenneaux, M. and Steeds, R., 2014. Reference values for mitral and tricuspid annular dimensions using two-dimensional echocardiography. *Echo Research and Practice*, 1(2), pp.43-50.
- Dziadzko, V. and Enriquez-Sarano, M., 2016. ISOLATED MITRAL REGURGITATION IN THE POPULATION: PREVALENCE AND OUTCOMES. *Journal of the American College of Cardiology*, 67(13), p.2188.
- Eckert, C., Fan, R., Mikulis, B., Barron, M., Carruthers, C., Friebe, V., Vyavahare, N. and Sacks, M., 2013. On the biomechanical role of glycosaminoglycans in the aortic heart valve leaflet. *Acta Biomaterialia*, 9(1), pp.4653-4660.
- Feher, J., 2013. *Quantitative Human Physiology: An Introduction*. Elsevier AP, pp.451-471.
- Finsberg, H., Xi, C., Zhao, X., Tan, J., Genet, M., Sundnes, J., Lee, L., Zhong, L. and Wall, S., 2019. Computational quantification of patient-specific changes in ventricular dynamics associated with pulmonary hypertension. *American Journal of Physiology-Heart and Circulatory Physiology*, 317(6), pp.H1363-H1375.
- Fox, D. and Khattar, R., 2006. Pulmonary arterial hypertension: classification, diagnosis and contemporary management. *Postgraduate Medical Journal*, 82(973), pp.717-722.
- Fujimoto, N., Hastings, J., Bhella, P., Shibata, S., Gandhi, N., Carrick-Ranson, G., Palmer, D. and Levine, B., 2012. Effect of ageing on left ventricular compliance and distensibility in healthy sedentary humans. *The Journal of Physiology*, 590(8), pp.1871-1880.
- Gaasch, W. and Meyer, T., 2008. Left Ventricular Response to Mitral Regurgitation. *Circulation*, 118(22), pp.2298-2303.
- Galiè, N., Humbert, M. and Vachiery, J., 2015. "2015 ESC/ERS Guidelines for the diagnosis and treatment of pulmonary hypertension. The Joint Task Force for the Diagnosis and Treatment of Pulmonary Hypertension of the European Society of Cardiology (ESC) and the European Respiratory Society (ERS)". *European Respiratory Journal*, 46(6), pp.1855-1856.
- Genet, M., Lee, L., Ballairgeon, B., Guccione, J. and Kuhl, E., 2015. Modeling Pathologies of Diastolic and Systolic Heart Failure. *Annals of Biomedical Engineering*, 44(1), pp.112-27.
- Giusca, S., Jurcut, R., Gingham, C. and Voigt, J., 2010. The right ventricle: anatomy, physiology and functional assessment. *Acta Cardiologica*, 65(1), pp.67-77.

- Göktepe, S., Abilez, O., Parker, K. and Kuhl, E., 2010. A multiscale model for eccentric and concentric cardiac growth through sarcomerogenesis. *Journal of Theoretical Biology*, 265(3), pp.433-442.
- Guccione, J., McCulloch, A. and Waldman, L., 1991. Passive Material Properties of Intact Ventricular Myocardium Determined from a Cylindrical Model. *Journal of Biomechanical Engineering*, 113(1), pp.42-55.
- Guccione, J., Moonly, S., Moustakidis, P., Costa, K., Moulton, M., Ratcliffe, M. and Pasque, M., 2001. Mechanism underlying mechanical dysfunction in the border zone of left ventricular aneurysm: a finite element model study. *The Annals of Thoracic Surgery*, 71(2), pp.654-662.
- Hampton, J. and Hampton, J., 2001. *The ECG Made Easy*. 5th ed. Edinburgh: Churchill Livingstone.
- Hoepfer, M., Humbert, M., Souza, R., Idrees, M., Kawut, S., Sliwa-Hahnle, K., Jing, Z., Simon, J., Gibbs, R., 2016. A global view of pulmonary hypertension. *Lancet Respiratory Medicine*, 4(4), pp.306-322.
- Hoepfer, M. and Humbert, M., 2019. The new haemodynamic definition of pulmonary hypertension: evidence prevails, finally!. *European Respiratory Journal*, 53(3), p.1900038.
- Holzapfel, G., Gasser, T. and Ogden, R., 2000. A New Constitutive Framework for Arterial Wall Mechanics and a Comparative Study of Material Models. *Journal of Elasticity and the Physical Science of Solids*, 61, pp.1-48.
- Holzapfel, G. and Ogden, R., 2009. Constitutive modelling of passive myocardium: a structurally based framework for material characterization. *Philosophical Transactions of the Royal Society A: Mathematical, Physical and Engineering Sciences*, 367(1902), pp.3445-3475.
- Huikuri, H., 1983. Effect of mitral valve replacement on left ventricular function in mitral regurgitation. *Heart*, 49(4), pp.328-333.
- Humbert, M., 2010. Pulmonary arterial hypertension and chronic thromboembolic pulmonary hypertension: pathophysiology. *European Respiratory Review*, 19(115), pp.59-63.
- Hunter, P., McCulloch, A. and ter Keurs, H., 1998. Modelling the mechanical properties of cardiac muscle. *Progress in Biophysics and Molecular Biology*, 69(2-3), pp.289-331.

- Hurtado, D. and Kuhl, E., 2012. Computational modelling of electrocardiograms: repolarisation and T-wave polarity in the human heart. *Computer Methods in Biomechanics and Biomedical Engineering*, 17(9), pp.986-996.
- Izumi, J., Iga, K., and Konishi, T., 2002. Progression of isolated tricuspid regurgitation late after mitral valve surgery for rheumatic mitral valve disease. *Journal of Heart Valve Disease*, 11(03), pp. 353-356.
- Jurcut, R., Giusca, S., Ticulescu, R., Popa, E., Amzulescu, M., Gheorghiu, I., Coman, I., Popescu, B., Voigt, J. and Ghingina, C., 2011. Different Patterns of Adaptation of the Right Ventricle to Pressure Overload: A Comparison between Pulmonary Hypertension and Pulmonary Stenosis. *Journal of the American Society of Echocardiography*, 24(10), pp.1109-1117.
- Kaul, S., Tei, C., Hopkins, J. and Shah, P., 1984. Assessment of right ventricular function using two-dimensional echocardiography. *American Heart Journal*, 107(3), pp.526-531.
- Kheifets, V., O'Dell, W., Smith, T., Reilly, J. and Finol, E., 2013. Considerations for Numerical Modeling of the Pulmonary Circulation—A Review with a Focus on Pulmonary Hypertension. *Journal of Biomechanical Engineering*, 135(6).
- Khoiy, K. and Amini, R., 2016. On the Biaxial Mechanical Response of Porcine Tricuspid Valve Leaflets. *Journal of Biomechanical Engineering*, 138(10).
- Knio, Z., Montealegre-Gallegos, M., Yeh, L., Chaudary, B., Jeganathan, J., Matyal, R., Khabbaz, K., Liu, D. and Senthilnathan, V., Mahmood, F., 2016. Tricuspid annulus: A spatial and temporal analysis. *Annals of Cardiac Anasthesia*, 19(4), p.599.
- Koelling, T., Aaronson, K., Cody, R., Bach, D. and Armstrong, W., 2002. Prognostic significance of mitral regurgitation and tricuspid regurgitation in patients with left ventricular systolic dysfunction. *American Heart Journal*, 144(3), pp.524-529.
- Kong, F., Pham, T., Martin, C., McKay, R., Primiano, C., Hashim, S., Kodali, S. and Sun, W., 2018. Finite Element Analysis of Tricuspid Valve Deformation from Multi-slice Computed Tomography Images. *Annals of Biomedical Engineering*, 46(8), pp.1112-1127.
- Kotikanyadanam, M., Göktepe, S. and Kuhl, E., 2010. Computational modeling of electrocardiograms: A finite element approach toward cardiac excitation. *International Journal for Numerical Methods in Biomedical Engineering*.
- Kunzelman, K.S., and R. P. Cochran, "Mechanical Properties of Basal and Marginal Mitral Valve Chordae Tendineae," *ASAIO Transactions*, 1990 Jul-Sep;36(3), pp.M405-8.

- Leary, P., Kurtz, C., Hough, C., Waiss, M., Ralph, D. and Sheehan, F., 2012. Three-Dimensional Analysis of Right Ventricular Shape and Function in Pulmonary Hypertension. *Pulmonary Circulation*, 2(1), pp.34-40.
- Lee, C., Laurence, D., Ross, C., Kramer, K., Babu, A., Johnson, E., Hsu, M., Aggarwal, A., Mir, A., Burkhart, H., Towner, R., Baumwart, R. and Wu, Y., 2019. Mechanics of the Tricuspid Valve—From Clinical Diagnosis/Treatment, In-Vivo and In-Vitro Investigations, to Patient-Specific Biomechanical Modeling. *Bioengineering*, 6(2), p.47.
- Lin, F., Devereux, R., Roman, M., Meng, J., Jow, V., Jacobs, A., Weinsaft, J., Shaw, L., Berman, D., Callister, T. and Min, J., 2008. Cardiac Chamber Volumes, Function, and Mass as Determined by 64-Multidetector Row Computed Tomography. *JACC: Cardiovascular Imaging*, 1(6), pp.782-786.
- Lisi, M., Cameli, M., Righini, F., Malandrino, A., Tacchini, D., Focardi, M., Tsioulpas, C., Bernazzali, S., Tanganelli, P., Maccherini, M., Mondillo, S. and Henein, M., 2015. RV Longitudinal Deformation Correlates with Myocardial Fibrosis in Patients with End-Stage Heart Failure. *JACC: Cardiovascular Imaging*, 8(5), pp.514-522.
- Liu, W. and Wang, Z., 2019. Current Understanding of the Biomechanics of Ventricular Tissues in Heart Failure. *Bioengineering*, 7(1), p.2.
- Lungu, A., Swift, A., Capener, D., Kiely, D., Hose, R. and Wild, J., 2016. Diagnosis of Pulmonary Hypertension from Magnetic Resonance Imaging–Based Computational Models and Decision Tree Analysis. *Pulmonary Circulation*, 6(2), pp.181-190.
- Mauger, C., Gilbert, K., Lee, A., Sanghvi, M., Aung, N., Fung, K., Carapella, V., Piechnik, S., Neubauer, S., Petersen, S., Suinesiaputra, A. and Young, A., 2019. Right ventricular shape and function: cardiovascular magnetic resonance reference morphology and biventricular risk factor morphometrics in UK Biobank. *Journal of Cardiovascular Magnetic Resonance*, 21(1).
- May-Newman, K. and Yin, F., 1995. Biaxial mechanical behavior of excised porcine mitral valve leaflets. *American Journal of Physiology-Heart and Circulatory Physiology*, 269(4), pp.H1319-H1327
- McLaughlin, V., Archer, S., Badesch, D., Barst, R., Farber, H., Lindner, J., Mathier, M., McGoon, M., Park, M., Rosenson, R., Rubin, L., Tapson, V. and Varga, J., 2009. ACCF/AHA 2009 Expert Consensus Document on Pulmonary Hypertension. *Circulation*, 119(16), pp.2250-2294.
- Mertens, L. and Hunter, K., 2012. Imaging right ventricular shape and remodeling. *European Heart Journal - Cardiovascular Imaging*, 14(4), pp.311-312.

- Modin, D., Møgelvang, R., Andersen, D. and Biering-Sørensen, T., 2019. Right Ventricular Function Evaluated by Tricuspid Annular Plane Systolic Excursion Predicts Cardiovascular Death in the General Population, *Journal of the American Heart Association*, 8(10).
- Morgan, A., et al., 2020. Imaging and computational modeling of tricuspid regurgitation and repair. *Vessel Plus*, 4(6).
- Naeije, R. and Dedobbeleer, C., 2013. Pulmonary hypertension and the right ventricle in hypoxia. *Experimental Physiology*, 98(8), pp.1247-1256.
- Nishimura, R., Otto, C., Bonow, R., Carabello, B., Erwin, J., Guyton, R., O'Gara, P., Ruiz, C., Skubas, N., Sorajja, P., Sundt, T. and Thomas, J., 2014. 2014 AHA/ACC Guideline for the Management of Patients with Valvular Heart Disease: Executive Summary. *Circulation*, 129(23), pp.2440-2492.
- Palumbo, M., Bandera, F., Caiani, E., Alfonzetti, E. and Guazzi, M., 2018. Computational Analysis of Right Ventricular Curvature by 3D Echocardiography: Implications on Pulmonary Hypertension Severity. *Journal of the American College of Cardiology*, 71(11), p.A1618.
- Pewowaruk, R., Philip, J., Tewari, S., Chen, C., Nyaeme, M., Wang, Z., Tabima, D., Baker, A., Beard, D. and Chesler, N., 2018. Multiscale Computational Analysis of Right Ventricular Mechanoenergetics. *Journal of Biomechanical Engineering*, 140(8).
- Pierce, E., Bloodworth, C., Imai, A., Okamoto, K., Saito, Y., Gorman, R., Gorman, J. and Yoganathan, A., 2018. Mitral annuloplasty ring flexibility preferentially reduces posterior suture forces. *Journal of Biomechanics*, 75, pp.58-66.
- Pfannmüller, B., Doenst, T., Eberhardt, K., Seeburger, J., Borger, M. and Mohr, F., 2012. Increased risk of dehiscence after tricuspid valve repair with rigid annuloplasty rings. *The Journal of Thoracic and Cardiovascular Surgery*, 143(5), pp.1050-1055.
- Pham, T., Sulejmani, F., Shin, E., Wang, D. and Sun, W., 2017. Quantification and comparison of the mechanical properties of four human cardiac valves. *Acta Biomaterialia*, 54, pp.345-355.
- Rausch, M., Dam, A., Göktepe, S., Abilez, O. and Kuhl, E., 2010. Computational modeling of growth: systemic and pulmonary hypertension in the heart. *Biomechanics and Modeling in Mechanobiology*, 10(6), pp.799-811.
- Sahli Costabal, F., Hurtado, D. and Kuhl, E., 2016. Generating Purkinje networks in the human heart. *Journal of Biomechanics*, 49(12), pp.2455-2465.

- Samad, B., Alam, M. and Jensen-Urstad, K., 2002. Prognostic impact of right ventricular involvement as assessed by tricuspid annular motion in patients with acute myocardial infarction. *The American Journal of Cardiology*, 90(7), pp.778-781.
- Shapiro, B., Nishimura, R., McGoon, M. and Redfield, M., 2006. Diagnostic Dilemmas: Diastolic Heart Failure Causing Pulmonary Hypertension and Pulmonary Hypertension Causing Diastolic Dysfunction. *Advances in Pulmonary Hypertension*, 5(1), pp.13-20.
- Shiels, H. and White, E., 2008. The Frank-Starling mechanism in vertebrate cardiac myocytes. *Journal of Experimental Biology*, 211(13), pp.2005-2013.
- Shuhaiber, J., 2018. Tricuspid valve annulus surgery during mitral valve surgery. *Journal of Thoracic Disease*, 10(6), pp.3156-3157.
- Singh-Gryzbon, S., Sadri, V., Toma, M., Pierce, E., Wei, Z. and Yoganathan, A., 2019. Development of a Computational Method for Simulating Tricuspid Valve Dynamics. *Annals of Biomedical Engineering*, 47(6), pp.1422-1434.
- Streeter, D., Spotnitz, H., Patel, D., Ross, J. and Sonnenblick, E., 1969. Fiber Orientation in the Canine Left Ventricle during Diastole and Systole. *Circulation Research*, 24(3), pp.339-347.
- Ton-Nu, T., Levine, R., Handschumacher, M., Dorer, D., Yosefy, C., Fan, D., Hua, L., Jiang, L. and Hung, J., 2006. Geometric Determinants of Functional Tricuspid Regurgitation. *Circulation*, 114(2), pp.143-149.
- Ueti, O., Carmago, E., Ueti, A., de Lima-Filho, E. and Nogueira, E., 2002. Assessment of right ventricular function with Doppler echocardiographic indices derived from tricuspid annular motion: comparison with radionuclide angiography. *Heart*, 88(3), pp.244-248.
- van de Veerdonk, M., Bogaard, H. and Voelkel, N., 2016. The right ventricle and pulmonary hypertension. *Heart Failure Reviews*, 21(3), pp.259-271.
- Vander, A., Widmaier, E., Raff, H., Strang, K. and Shoeppe, T., 2011. *Vander's Human Physiology*. 12th ed. McGraw-Hill.
- Verdonk, C., Darmon, A., Cimadevilla, C., Lepage, L., Raffoul, R., Nataf, P., Vahanian, A. and Messika-Zeitoun, D., 2018. Is tricuspid annuloplasty increasing surgical mortality and morbidity during mitral valve replacement? A single-centre experience. *Archives of Cardiovascular Diseases*, 111(8-9), pp.480-486.
- Walker, J., Ratcliffe, M., Zhang, P., Wallace, A., Fata, B., Hsu, E., Saloner, D. and Guccione, J., 2005. MRI-based finite-element analysis of left ventricular aneurysm. *American Journal of Physiology-Heart and Circulatory Physiology*, 289(2), pp.H692-H700.

Wei, J., Chang, C., Lee, F. and Lai, W., 1993. De Vega's semicircular annuloplasty for tricuspid valve regurgitation. *The Annals of Thoracic Surgery*, 55(2), pp.482-485.

Weese, J., Smith, N., Razavi, R., Chapelle, D., Delingette, H., Frangi, A., Hose, R., Hunter, P. and Spaan, J., 2013. [online] Euheart.eu. Available at:
<http://www.euheart.eu/fileadmin/system/euheart/documents/euHeart_report.pdf>
[Accessed 21 April 2020].

Xi, C., Latnie, C., Zhao, X., Tan, J., Wall, S., Genet, M., Zhong, L. and Lee, L., 2016. Patient-Specific Computational Analysis of Ventricular Mechanics in Pulmonary Arterial Hypertension. *Journal of Biomechanical Engineering*, 138(11).

Appendix

1.1 Overview of Continuum Models

The most fundamental operations on vectors involve: the dot product, which reduces the order of the vector to a scalar; the cross product, which conserves the order of the vector; and the dyadic, which increases the order of the vector. Here, we will represent the scalars in lower case e.g. a , vectors in bolded lowercase e.g. \mathbf{a} , and tensors in bolded uppercase e.g.

A. Given vector \mathbf{u} and \mathbf{v} ,

- Dot product

$$\mathbf{u} \cdot \mathbf{v} = [u_1 \quad u_2 \quad u_3] \begin{bmatrix} v_1 \\ v_2 \\ v_3 \end{bmatrix} = u_1 v_1 + u_2 v_2 + u_3 v_3;$$

- Cross Product

$$\mathbf{u} \times \mathbf{v} = (u_2 v_3 - u_3 v_2) \mathbf{e}_1 + (u_3 v_1 - u_1 v_3) \mathbf{e}_2 + (u_1 v_2 - u_2 v_1) \mathbf{e}_3;$$

Where \mathbf{e}_1 , \mathbf{e}_2 and \mathbf{e}_3 are orthogonal unit base vectors.

- Dyadic

$$\mathbf{u} \otimes \mathbf{v} = \begin{bmatrix} u_1 \\ u_2 \\ u_3 \end{bmatrix} [v_1 \quad v_2 \quad v_3] = \begin{bmatrix} u_1 v_1 & u_1 v_2 & u_1 v_3 \\ u_2 v_1 & u_2 v_2 & u_2 v_3 \\ u_3 v_1 & u_3 v_2 & u_3 v_3 \end{bmatrix};$$

In continuum mechanics, the deformation gradient \mathbf{F} , describes the deformation between a position vector defined in the reference configuration, $d\mathbf{X}$, and the corresponding orientation on the deformed orientation, $d\mathbf{x}$:

$$d\mathbf{x} = \mathbf{F}d\mathbf{X};$$

Or

$$\begin{bmatrix} dx_1 \\ dx_2 \\ dx_3 \end{bmatrix} = \begin{bmatrix} F_{11} & F_{12} & F_{13} \\ F_{21} & F_{22} & F_{23} \\ F_{31} & F_{32} & F_{33} \end{bmatrix} \begin{bmatrix} dX_1 \\ dX_2 \\ dX_3 \end{bmatrix};$$

The deformation gradient, \mathbf{F} , can be decomposed into a rotation component \mathbf{R} , and a stretch component, \mathbf{U} :

$$\mathbf{F} = \mathbf{R}\mathbf{U};$$

With Rigid Body Rotation having $\mathbf{U} = \mathbf{I}$; and pure stretch having $\mathbf{R} = \mathbf{I}$. The Jacobian, J , is computed from \mathbf{F} as $J = \det(\mathbf{F})$ and $J > 1$. In incompressible materials, $J = 1$. Stretch can be defined as $\lambda = |\boldsymbol{\lambda}_a|$:

$$\boldsymbol{\lambda}_a = \mathbf{F}\mathbf{a}_0;$$

Where \mathbf{a}_0 is a unit vector between two points on the reference material. Therefore:

$$\lambda^2 = \boldsymbol{\lambda}_a \cdot \boldsymbol{\lambda}_a = (\mathbf{F}\mathbf{a}_0) \cdot (\mathbf{F}\mathbf{a}_0);$$

$$\lambda^2 = (\mathbf{a}_0\mathbf{F}^T) \cdot (\mathbf{F}\mathbf{a}_0) = \mathbf{a}_0 \cdot (\mathbf{C}\mathbf{a}_0);$$

Where \mathbf{C} is the right Cauchy-Green tensor. Since \mathbf{C} can describe deformation and is symmetric, we can use the principle components of \mathbf{C} to describe material deformations. The three principle invariants are:

$$I_1 = \text{trace}(\mathbf{C}), \quad I_2 = \frac{1}{2}(I_1^2 - \text{tr}(\mathbf{C}^2)), \quad I_3 = \det(\mathbf{C});$$

If the material contains favorable orientations, such as fibers in directions \mathbf{a}_0 and \mathbf{b}_0 in a composite, this can be accounted for with the invariants called pseudo-invariants, and are given by:

$$I_4 = \mathbf{a}_0 \cdot (\mathbf{C}\mathbf{a}_0), \quad I_5 = \mathbf{a}_0 \cdot (\mathbf{C}^2\mathbf{a}_0);$$

$$I_6 = \mathbf{b}_0 \cdot (\mathbf{C}\mathbf{b}_0), \quad I_7 = \mathbf{b}_0 \cdot (\mathbf{C}^2\mathbf{b}_0);$$

$$I_8 = \mathbf{a}_0 \cdot (\mathbf{C}\mathbf{b}_0);$$

Finally, it is important to construct the Strain Energy Function (SEF), $\Psi(\mathbf{C})$, from these invariants, and the choice of invariants and their roles depends on behavior determined experimentally. The Cauchy Stress for compressible and incompressible materials is defined as:

$$J\boldsymbol{\sigma} = \mathbf{F} \frac{\partial \Psi}{\partial \mathbf{F}} = \mathbf{F} \sum_{i=1}^N \psi_i \frac{\partial I_i}{\partial \mathbf{F}}, \quad \text{and} \quad \boldsymbol{\sigma} = \mathbf{F} \sum_{i=1}^N \psi_i \frac{\partial I_i}{\partial \mathbf{F}} - p\mathbf{I};$$

Where the Lagrangian Multiplier is used to enforce the incompressibility constraint ($J=1$).

1.2 Abaqus Implementation

The LHHM platform is an ABAQUS based FE Multiphysics solver. Electrical analysis uses an implicit *HEAT TRANSFER step, while the mechanical runs are solved using an explicit solver in the *DYNAMIC step. The geometry files consist of two major components:

- 1- The nodal coordinates. In the electrical run, nodes correspond to the End Diastolic Volumes and are contained in the Analysis input file (heart-elec.inp) in the below format:

*Node

```
"node label", "x coordinate", "y coordinate", "z coordinate"
```

In the mechanical file, (heart-mech.inp), the node coordinates are replaced by coordinates at a preloaded state (70% diastole) and this is to establish physiological chamber pressure at the End Diastolic geometry. These preloaded coordinates are stored in files named (e.g. nodes_VENTRICLES.inp) and are called in the analysis file in the line

*Nodes

```
*Include, input=nodes_VENTRICLES.inp
```

- 2- Fiber orientations are ascribed to the chambers as a discrete field and are stored in files (e.g. DF-VENTRICLES.inp). They are called in the same format

*Distribution

```
*Include, input= DF-VENTRICLES.inp
```

These local orientations are defined at element centroids and are written in the following format:

```
"element label", x1,y1,z1,x2,y2,z2
```

The first two global orientations are defined and ABAQUS infers the third from cross multiplication.

Material properties are defined in files (elec-mat-Ventricles.inp) or (mech-mat-LV_ACTIVE.inp). They are defined as previously started:

```
*Material, name=ACTIVE_LV  
*Include, input=mech-mat-LV_ACTIVE.inp
```

Assignment of thermal expansion on the local orientation can be done by adding the line

```
*Material, name=Expanded_Active_LV  
*Expansion, TYPE=ORTHO  
 $\alpha_{11}, \alpha_{22}, \alpha_{33}$   
*Include, input=mech-mat-LV_ACTIVE.inp
```

Connector Elements are defined on nodes under the *Assembly subsection:

```
*Element, type=CONN3D2  
    "element label", firstnode,secondnode  
*Connector Section, behavior=Stiffness-Pulmonary  
    Axial,
```

Where Stiffness-Pulmonary is defined as

```
*Connector Behavior, name=Stiffness-Pulmonary  
*Connector Elasticity, component=1  
    3.78143,
```

If the connector type is rigid, there is no need to define "behavior" and "Axial," will be substituted with "Rigid,"

1.3 Parameters Used in our model

Variables	Pre-Surgery		Post-Surgery			
	RV	LV	RV	LV	TV	MV
Density (kg/mm)	1.06 x 10 ⁻⁹				1.06 x 10 ⁻⁶	
Damping	160			300		
Passive Response						
a (MPa)	0.00335358		0.028	0.00087072	0.0018	
b	7.08			2.73		
a_f (MPa)	0.0025005		0.0025		0.0005	
b_f	5.34			12		
a_s (MPa)	0			0.00385		
b_{fs}	0			0.7599		
a_{fs} (MPa)	0			0.00385		
b_{fs}	0			0.7599		
D	0.1			4.29		
Active Response						
T_{max} (MPa)	0.8	0.7	0.35	0.4		
t_{θ} (s)	0.17					
m	238.35					
l_{θ} (mm)	0.00075					
b	-0.26					
B	4750					

Ca_{max}	4.35			
Ca_0	4.35			
n	0.4	0.9	0.4	0.9

1.4 Measured Raw Data Fitting/Shape Analysis

Fitted Data:

Preload (mmHg)	Temperature Applied (θ)	RA Volume (ml)
3.99783	35	181
3.99783	20	170
3.99783	20	170.2
3.99783	5	159
1.875155	0	131.9
1.650136	0	131.9
4.000081	0	155.106
3.000248	20	160.47
3.000248	0	146.7
1.875155	35	149.973
1.650136	20	138.589

The equation that was fitted was as follows:

$$\text{RA Volume} = 113.7 + 10.48 * p + 0.2694 * \theta + 0.1249 * p\theta + (-0.001041) * \theta^2$$

Goodness of Fit:

$$R^2 = 0.9976$$

$$SSE = 16.75$$

Model Predictions:

p	θ	Fitted	Measured
2.250186	0	137.3	137
1.875155	0	133.39	132
0.750062	0	121.6	97
0.750062	35	133.04	108

Shape Analysis results of MRI with series 14 and 17 used pre-surgery, and series 12 used post-surgery:

	Pre-surgery		Post-surgery	
	RV	LV	RV	LV
AB	71.73 mm	76.48 mm	67.70 mm	70.32 mm
MID	24.60 mm	49.56 mm	23.49 mm	44.36 mm
LA/RA	41.85 mm	56.40 mm	37.82 mm	50.19 mm
RV Bulge	15.77 mm	-	14.26 mm	-